Lund University

Master Thesis

Epitaxial growth and processing of high-aspect ratio InGaAs fins for advanced MOSFETs

Author:
Andreas Malmgren

Supervisor:
Dr. Mattias Borg

Lund
University

Nanoelectronics group
Department of Electrical and Information Technology, LTH

June 2017

LUND UNIVERSITY

Abstract

Faculty of Engineering
Department of Electrical and Information Technology, LTH

Master of Science

Epitaxial growth and processing of high-aspect ratio InGaAs fins for advanced MOSFETs

by Andreas Malmgren

In this thesis, InGaAs fins with vertical sidewalls consisting of {110} facets were epitaxially grown on InP(111)B substrates using metalorganic vapor phase epitaxy. A lithography patterned hydrogen silsesquixane growth mask was used to promote the formation of vertical {110} facets during the growth. The relative growth rate of the {111}B and {110} facets was controlled by the input V/III ratio in the gas phase. It was found that for low V/III ratios, high InGaAs fins with minimal mask overgrowth could be grown. Facet selective growth of InGaAs fins on InP(111)B can thus be used to fabricate the channel in modern fin field-effect transistors (FinFETs). Prior to the growth of InGaAs fins, the chemical composition of epitaxially grown $In_xGa_{1-x}As$ films on different InP substrates was measured using reciprocal space mapping. The purpose of this was to calibrate the InGaAs growth in terms of chemical composition on various crystal facets. Several thin $In_xGa_{1-x}As$ films were grown at 600°C using trimethyl gallium, trimethyl indium, and arsine. The results revealed that the chemical composition of $In_xGa_{1-x}As$ on InP(111)B, InP(110), and InP(001) differed considerably when grown during identical conditions. It was found that thin InGaAs films of good crystal quality could be grown on InP(111)B and InP(001) during these conditions. The growth on InP(110) during the same conditions resulted in relaxed gallium rich InGaAs films.

Acknowledgements

I would like to express great gratitude towards my supervisor Mattias Borg who has provided me with guidance and inspiration throughout this project. Mattias introduced me to the Lund Nano Lab cleanroom and provided me with lots of practical and theoretical knowledge regarding epitaxy and high resolution x-ray diffraction (HRXRD). I would also like to thank the rest of the members of the Nanoelectronics group at the department of electrical and information technology at the technical faculty (EIT LTH) for all the help and support. I am especially grateful towards Cezar Zota who many times acted as my practical coach regarding almost anything in and outside of the lab. I am also very thankful towards Fredrik Lindelöw, Adam Jönsson, Olli-Pekka Kilpi, and Elvedin Memisevic for teaching me how to operate electron beam lithography (EBL), scanning electron microscopy (SEM), and focused ion beam (FIB) as well as how to handle chemicals. Also, a special thanks to Peter Blomqvist, Anders Kvennefors, and Dmitry Suyatin from the Lund Nano Lab staff who helped me with issues regarding equipment in the lab. I would also like to thank Filip Lenrick for teaching me the procedure of FIB milling. A big thanks also goes to my fellow master students Christian Möhle, Albin Linder, Edvin Winqvist, Daniel Svedbrand, George Gioulis and Lun Sang with whom I spent many hours in the office with. Last but certainly not least, I would like to thank my parents Anders and Marita as well as my sister Louise for their moral support and interest.

Contents

Abstract **i**

Acknowledgements **ii**

Contents **iii**

Abbreviations **v**

Symbols **vii**

1 Background and introduction **1**
1.1 The MOSFET . . . 1
1.1.1 MOSFET operation . . . 1
1.1.2 The FinFET design . . . 2
1.1.3 Scaling issues of planar MOSFETs . . . 3
1.1.4 The advantage of FinFETs . . . 3
1.1.5 History of FinFETs . . . 4
1.1.6 Fabrication of fins for FinFETs . . . 4
1.1.7 Alternative fabrication methods . . . 5
1.2 Motivation and purpose . . . 6

2 Theory **8**
2.1 Crystallography of III-V semiconductors . . . 8
2.2 Metalorganic vapor phase epitaxy . . . 9
2.2.1 MOVPE setup . . . 10
2.3 Scanning electron microscopy and focused ion beam . . . 11
2.3.1 Focused ion beam . . . 12
2.4 Lithography . . . 12
2.4.1 Resists in electron beam lithography . . . 13
2.4.2 Spin coating of resists . . . 13
2.4.3 HSQ e-beam resist . . . 13
2.4.4 EBL exposure . . . 14
2.4.5 Controlling the dose in EBL . . . 14
2.4.6 Development of resists . . . 15

2.5 Strain in epitaxial films . . . 16
2.6 High resolution X-ray diffraction . . . 17
2.6.1 Bragg's law . . . 18
2.6.2 Diffraction in reciprocal space . . . 20

3 Experimental methods 22
3.1 Reciprocal space mapping . . . 22
3.1.1 Position sensitive detectors . . . 24
3.2 Facet selective growth . . . 24
3.2.1 Facets on InP(111)B . . . 25
3.2.2 Growth of fins using a growth mask . . . 25

4 Results and discussion 27
4.1 Epitaxial growth calibration of InGaAs films . . . 27
4.2 Reciprocal space mapping and composition evaluation . . . 29
4.2.1 InGaAs films on InP(111)B . . . 29
4.2.2 InGaAs films on InP(001) . . . 32
4.2.3 InGaAs films on InP(110) . . . 34
4.2.4 Comparison of growth behaviors on InP . . . 36
4.3 Preparation of the growth mask . . . 38
4.4 Facet selective growth of InGaAs fins . . . 39
4.4.1 Impact of growth mask orientation . . . 39
4.4.2 Misaligned growth mask . . . 41
4.4.3 FIB cross sections . . . 42
4.4.4 Growth of higher fins . . . 43
4.4.5 Possible issues of the facet selective growth . . . 45

5 Conclusion and outlook 48

A Modeling the critical thickness of InGaAs on InP 50

B Formation of the growth mask 53
B.1 Resist spin coating . . . 53
B.2 Patterning . . . 53
B.3 Development . . . 54

Bibliography 56

Abbreviations

MOS	metal-oxide-semiconductor
MOSFET	metal-oxide-semiconductor field-effect transistor
FinFET	fin field-effect transistor
InGaAs	indium gallium arsenide
InP	indium phosphide
EIT	department of electrical and information technology
LTH	technical faculty at Lund university
CMOS	complementary metal-oxide-semiconductor
FCC	face centered cubic
MOVPE	metalorganic vapor phase epitaxy
SCCM	standard cubic centimeters per minute
TMIn	trimethyl indium
TMGa	trimethyl gallium
SEM	scanning electron microscope/microscopy
FIB	focused ion beam
EBL	electron beam lithography
HSQ	hydrogen silsesquixane
PMMA	poly(methyl methacrylate)
TMAH	tetramethylammonium hydroxide
HRXRD	high resolution x-ray diffraction
RSM	reciprocal space mapping/map
GaAs	gallium arsenide
PSD	position sensitive detector
MIBK	methyl isobutyl ketone

BOE	buffered oxide etch
PL	photoluminescence

Symbols

a	lattice constant	Å
p	pressure	Torr
h	thickness	Å
G	sheer modulus	pascal
b	Burgers vector	Å
h_c	critical thickness	Å
n	integer	
d_{hkl}	interplanar spacing	Å
$\vec{S}_{hkl}$	reciprocal lattice vector	$Å^{-1}$
$\vec{k}_i$	incident x-ray vector	$Å^{-1}$
$\vec{k}_f$	reflected x-ray vector	$Å^{-1}$
$\vec{Q}_{hkl}$	diffraction vector	$Å^{-1}$
Φ	gas flow	sccm
$\Delta\phi$	shift during tetragonal distortion	$^\circ$
ν	Poisson ratio	
ϵ	lattice mismatch	
λ	wavelength	Å
θ	Bragg angle	$^\circ$
2θ	detector angle	$^\circ$
ω	incident x-ray angle	$^\circ$

Chapter 1

Background and introduction

1.1 The MOSFET

A metal-oxide-semiconductor field-effect transistor (MOSFET) is a type of transistor that consists of a metal-oxide-semiconductor (MOS) capacitor connected to three metal contacts called source, gate, and drain. Figure 1.1 shows a MOSFET in which the MOS capacitor is built on a semiconducting substrate. An insulating material, usually an oxide, is located between the metal gate contact and the semiconductor thus forming the MOS capacitor. The source and drain contacts are located next to the MOS capacitor on the semiconductor. This design is called planar design and is one of many ways to fabricate MOSFETs.

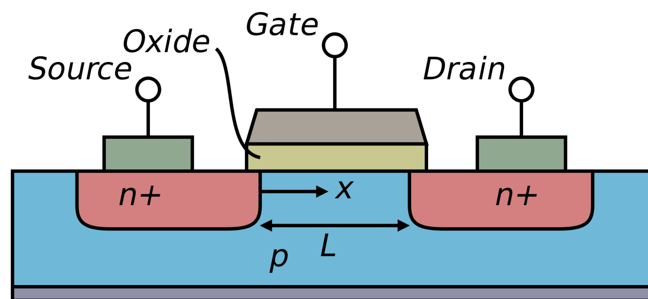

FIGURE 1.1: A cross section of a conventional planar MOSFET.

1.1.1 MOSFET operation

The purpose of a MOSFET is to control the current that flows between the source and drain contacts by an external voltage, that is, the gate voltage. As a gate

voltage is applied, a conductive channel is formed in the semiconductor near the semiconductor-oxide interface. A voltage between the source and drain contacts can then be used to drive a current through the formed channel in the semiconductor, called the drain current. The drain current can only flow when the channel is formed, that is, when a gate voltage is applied. In the absence of a gate voltage, no channel is formed and hence no drain current can flow no matter the voltage between the source and drain. The purpose of the drain voltage is to drive the current through the channel whereas the gate voltage controls how much current is allowed to flow. By changing the gate voltage, the conductive channel is either further opened or further closed which regulates the drain current. In a MOSFET, the drain current is thus not controlled by the voltage between the source and drain terminals that it actually flows. This makes MOSFETs useful for applications that involves amplification and on/off switching of electrical signals. Small changes in the gate voltage can result in large changes in the drain current which is why MOSFETs are attractive for the amplification of weak signals. Additionally, the drain current can be switched on and off very fast by changing the gate voltage between two set-point values. This fast switching behavior is utilized in logic complementary metal-oxide-semiconductor (CMOS) circuits which are used to build microprocessors.

1.1.2 The FinFET design

As mentioned earlier, the planar MOSFET design is just one of many ways to fabricate a MOSFET. A more modern and advanced design is the fin field-effect transistor (FinFET) design. The main difference between planar MOSFETs and FinFETs is the geometrical shape of the devices. Figure 1.2 a) illustrates the geometry of a planar MOSFET where L_g and W_g represents the length and width of the gate respectively. In planar MOSFETs, the channel is buried within the semiconducting substrate whereas the oxide and gate contact are deposited on top of the substrate. For a FinFET which is shown in figure 1.2 b), the channel consists of a 3-dimensional "fin" with height H_{fin} and width W_{fin} that runs along the surface of the substrate. The 3-dimensional fin allows for the oxide and gate contact to be wrapped around the channel thus providing gate coverage from three sides compared to only one side in planar MOSFETs.

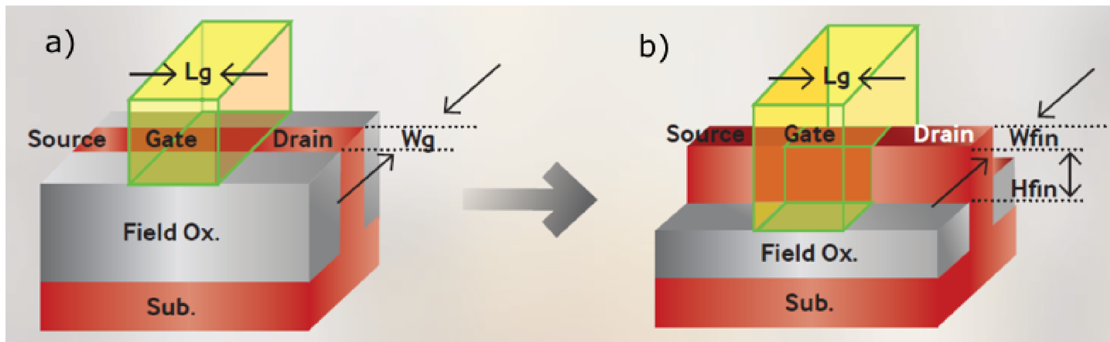

FIGURE 1.2: The device geometry of a) a planar MOSFET and b) a FinFET.

1.1.3 Scaling issues of planar MOSFETs

As the gate length is scaled in planar MOSFETs, the distance between the source and drain becomes smaller leading to a shorter channel. As a result, the gate loses control of the channel and the transistor becomes more difficult to turn off. This is because the electric field between the closely spaced source and drain regions has gained unwanted control of the channel. This is an example of a so called short channel effect which means that the applied gate voltage no longer entirely controls the channel. When short channel effects are present, the source-drain voltage also controls the channel and can regulate the drain current. This means that when no gate voltage is applied, a small drain current can still flow through the channel due to the source-drain voltage. This is highly unwanted and leads to reduced performance of the transistor in terms of energy consumption since the channel cannot completely be turned off. This is a big concern in modern integrated CMOS chips which consists of billions of transistors where the leakage current from each transistor leads to increased energy consumption of the entire chip.

1.1.4 The advantage of FinFETs

By using a FinFET design, short channel effects and leakage currents can be more efficiently suppressed than in planar MOSFETs as the gate length is scaled. This is attributed to the large gate coverage in FinFETs which is advantageous since the gate is coupled to the channel trough capacitive effects through the MOS interface. The electrostatic control that the gate has over the channel is thus enhanced in FinFETs by having the channel surrounded by the gate from three sides compared to only one side in planar MOSFETs. FinFETs are therefore

more immune to short channel effects and can turn off the conducting channel more efficient thus reducing leakage currents.

Besides from being more immune to short channel effects, FinFETs also has the possibility to obtain higher drain currents when the transistor is turned on. This is controlled by the height and width of the fin since a larger cross sectional area of the fin leads to a higher drain current for a specific drain current density. High drain currents are beneficial for both amplification and switching purposes in order to obtain high output signals and to distinguish between an on and off state of the transistor.

1.1.5 History of FinFETs

The research of FinFETs began in the early 2000's and the advantages compared to planar MOSFETs quickly became clear [1, 2]. The enhanced electrostatic gate control in FinFETs allowed for further scaling of the CMOS technology and thus a continuation of Moore's law [3]. In 2011, the first commercial chips using FinFET CMOS technology were manufactured by Intel Corporation in their 22 nm production node [4]. As of today, many of the major chip manufacturers such as GlobalFoundries, Taiwan Semiconductor Manufacturing Company (TSMC), and Samsung Electronics have implemented the FinFET technology in their chips. Most microprocessors in modern electronic devices are therefore powered by FinFETs.

1.1.6 Fabrication of fins for FinFETs

The fabrication of fins in modern semiconductor production lines is carried out by a technique called dry etching which selectively etches fins in silicon substrates. In the dry etching process, a plasma of reactive gases is formed in a vacuum chamber where the ions in the plasma are accelerated by a high frequency electric field towards the substrate. As the ions hit the substrate, physical and chemical etching occurs which results in the removal of silicon material to a certain depth within the substrate. The etching is performed selectively which means that only certain parts of the substrate is etched as shown in figure 1.3. The lithography patterned photomask in figure 1.3 acts a a protective layer which only exposes certain parts of the substrate to the etching plasma. The final etched pattern is

thus defined by the shape of the mask. For example, a mask consisting of closely spaced lines will result in etching of the substrate *between* the lines in the mask. The end result after removing the protective mask will then consist of etched trenches in the substrate which can be used as fins in the fabrication of FinFETs.

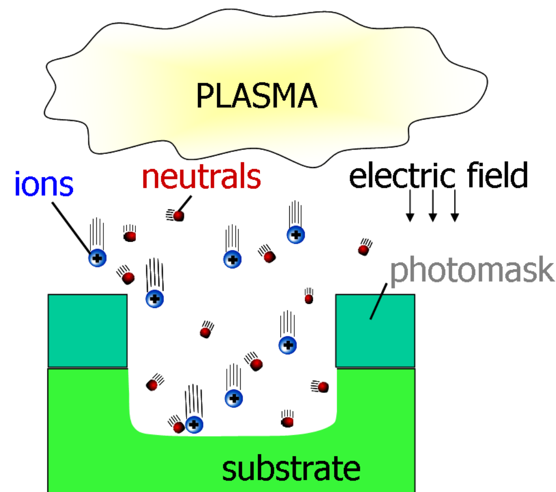

FIGURE 1.3: Illustrations of a dry etching process. The ions are accelerated towards the substrate surface where they etch material. The lithography patterned photomask defines the etched pattern.

1.1.7 Alternative fabrication methods

The concern with dry etching is the possibility to damage the surface of the fins in the plasma etching process [5]. As the ions in the plasma are used to etch material around the fins, the surface of the etched fins may potentially be damaged due to the ion bombardment. The issue of this is the creation of surface density states that may affect the carrier mobility and thus the electrical transport properties of the fins. This might lead to degraded performance of the final transistors in terms of current levels and energy consumption.

Alternative fin-formation methods that do not damage the fins during the fabrication process has been proposed [6, 7]. An example of a process that do not involve plasma etching is selective epitaxial growth [8–10]. Selective epitaxial growth means that the fins are grown epitaxially on the substrate using a mask where the shape of the fins is defined by crystal planes. In this fabrication process, the surface of the fins is not exposed to an etching plasma that inflicts damage and

degrades material properties. Epitaxially grown fins therefore have preserved electrical transport properties and low surface density states which allows FinFETs to operate at their full potential.

Selectively grown fins with high quality surfaces are especially important in FinFETs using III-V semiconductors as the fin material. This is because the high electron mobility offered by III-V semiconductors might be significantly downgraded in a fabrication process that involves plasma etching. High electron mobilities are beneficial since the electrons in the channel may travel at increased velocities that leads to higher currents. Any damage to the fins could lead to increased scattering of electrons in the channel and thus the potential current gain due to the high mobility would be lost. The performance gain by using III-V semiconductors in FinFETs may therefore be limited if the fins are damaged.

1.2 Motivation and purpose

Recent work carried out in the Nanoelectronics group at the department of electrical and information technology at the technical faculty at Lund university (EIT LTH) have demonsteratred high performance FinFETs with epitaxially grown InGaAs fins on InP(001) substrates [8–10]. The growth of the fins was found to be limited by the formation of {110} facets that were inclined at 45° with respect to the surface as shown in figure 1.4. As the {110} facets are formed, the original {001} facet on top of the fins disappear. This limits the total height of InGaAs fins grown on InP(001) since there are no facets on the fins that can grow vertically as the {110} facets have been formed.

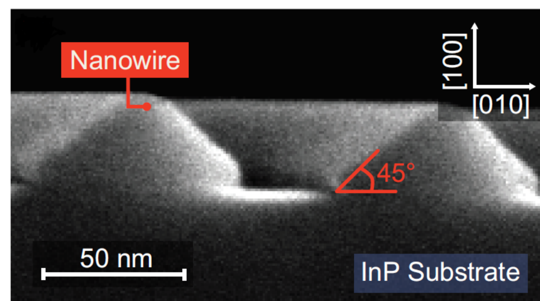

FIGURE 1.4: Epitaxially grown InGaAs fins on an InP(001) substrate where the sidewalls of the fins are limited by {110} facets [19]

.

An approach to grow high-aspect ratio InGaAs fins whose height is not limited by facets is therefore to grow on a different substrate. On InP(111)B, the {110} facets grow orthogonally to the [111]B direction and might therefore yield fins with vertical sidewalls. The purpose of this thesis is therefore to investigate the growth of high-aspect ratio InGaAs fins on InP(111)B substrates for the potential use in modern FinFETs.

Chapter 2

Theory

2.1 Crystallography of III-V semiconductors

Many III-V compound semiconductors crystallize in the *zincblende* crystal structure, among them InP and InGaAs [11, 12]. The zincblende crystal structure consists of two interpenetrating face centered cubic (fcc) lattices that are displaced relative to each other. Each fcc lattice has a lattice parameter a which is defined as the distance between the corner atoms in the corresponding fcc unit cell. The origin of the second fcc lattice is located at $\sqrt{3}/4 \cdot a$ along the cubic diagonal of the first fcc lattice. In the case of InP, one fcc lattice consists of indium atoms whereas the other contains phosphorus atoms. The entire zincblende structure is usually considered as a single fcc unit cell as shown in figure 2.1. The small and big spheres in figure 2.1 represents cations and anions respectively, or vice versa. Each cation and anion in the zincblende structure is tetrahedrally bonded to four ions of different polarity. As a result, $\{110\}$ planes of the zincblende structure contains an equal number of cations and anions and are thus non-polar planes since the charge is balanced. In contrast, the $\{100\}$ and $\{111\}$ planes of the zincblende structure contains only cations or anions and are called polar planes. For example, the [111] direction in zincblende structures have alternating (111) planes that contain either cations or anions only. Those planes are distinguishable and wafers with normal direction towards [111] are labeled either (111)A or (111)B where A denotes a surface of anions and B a surface of cations.

Due to the non-polar nature of the $\{110\}$ planes in zincblende structures, zincblende wafers often break along the $\{110\}$ planes. This is because the electrostatic force

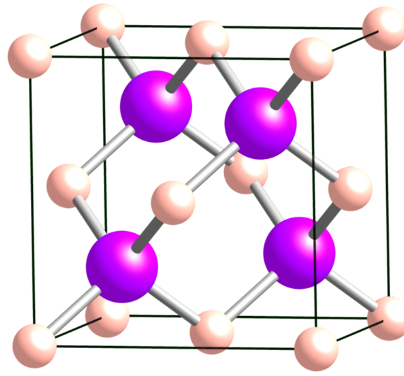

FIGURE 2.1: Illustration of the zincblende unit cell.

between {110} planes is weaker than between other planes. The force between {100} and {111} planes is greater due to the electrostatic force between A and B planes which makes it hard to cleave zincblende wafers along those planes.

2.2 Metalorganic vapor phase epitaxy

Metalorganic vapor phase epitaxy (MOVPE) is a technique used to epitaxially grow single or polycrystaline thin films. It is often used to grow heterostructures of III-V semiconductors [13]. It is most commonly performed at a total reactor pressure of 100 mbar and is then refereed to as low pressure MOVPE. MOVPE is a chemical process in which the materials to be grown are bonded to volatile organic molecules. Metals from group III such as indium and gallium are combined with organics such as methyl or ethyl leading to the formation of trimethyl indium (TMIn) or triethyl gallium (TEGa) [14]. These metalorganic compounds are liquids at room temperature and are stored in containers which are bubbled with hydrogen gas. The role of the hydrogen gas is to transport the metalorganic precursors as vapors to the reactor and is therefore called carrier gas. After reaching the heated substrate in the reactor, the metalorganic precursors thermally dissociate in the absence of oxygen, known as pyrolysis. This leaves the group III atoms on the surface of the substrate and allows for physical and chemical binding into the crystal lattice [15, 16]. Group V elements such as arsenic and phosphorus are treated similarly but do not necessarily have to be stored in liquid form and bubbled with a carrier gas. Hydrides which are binary compounds with hydrogen such as arsine (AsH_3) and phosphine (PH_3) are commonly used as precursors for the group V elements. The reason for this is to reduce the unintentional carbon

incorporation in the grown films due to incomplete decomposition of the metalorganic molecules. AsH_3 and PH_3 are stored as gases and are highly toxic and thus require extensive safety precautions.

2.2.1 MOVPE setup

The setup of an MOVPE system consists of several parts such as reactor, precursor storage, precursor transportation system, electronic control units, and pumps [17]. Figure 2.2 illustrates a typical MOVPE setup with a horizontal reactor and where the group III and group V precursors are alkyls and hydrides respectively. The group III precursors are stored in temperature controlled gas bubblers (denoted alkyl source in figure 2.2) in which the carrier gas is injected. The carrier gas is led through pipes to the bottom of the bubbler where it bubbles through the metalorganic liquid and picks up the metalorganic precursor. A gas outlet is located at the top of the bubbler where the bubbled metalorganic vapor and the carrier gas is vented and transported to the reactor. The amount of metalorganic vapor that is picked up by the carrier gas depends on the flow of the carrier gas as well as on the vapor pressure and temperature of the liquid. The vapor pressure is a function of temperature and is given by

$$log_{10}(p_v^{MO}) = B - A/T \tag{2.1}$$

where p_v^{MO} is the vapor pressure of the metalorganic in Torr, A and B are gas constants for the corresponding metalorganic in Torr, and T is the temperature of the liquid in kelvin.

The flow of the metalorganic vapor that leaves the bubbler is then given by

$$\Phi^{MO} = \frac{p_v^{MO}}{p_{bubbler} - p_v^{MO}} \cdot \phi_{carrier} \tag{2.2}$$

where Φ^{MO} is the flow of the metalorganic vapor in standard cubic centimeters per minute (sccm), $p_{bubbler}$ is the line pressure of the bubbler, and $\Phi_{carrier}$ is the flow of the injected carrier gas in sccm.

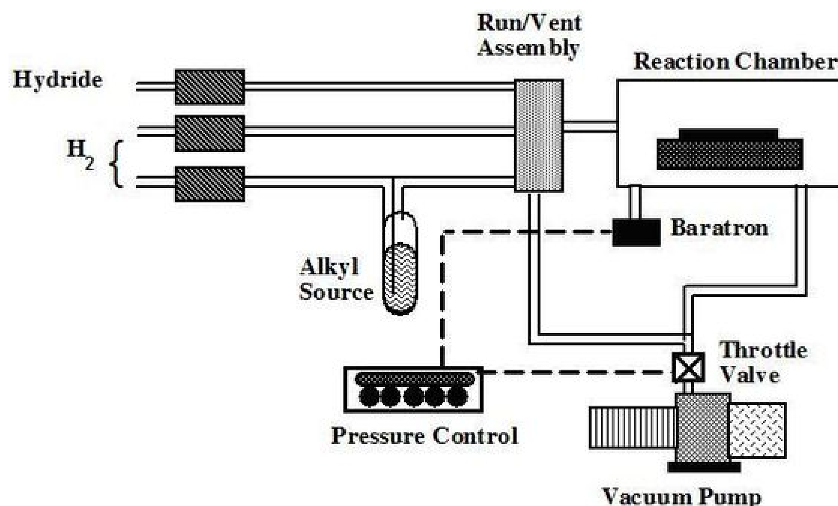

FIGURE 2.2: MOVPE setup with reactor and precursor transportation system.

2.3 Scanning electron microscopy and focused ion beam

Scanning electron microscopy (SEM) is a technique used to investigate nanoscale features on various surfaces. In comparison with optical microscopy where light is used to probe the surface, SEM uses electrons. The resolution of any microscope is related to the wavelength of the probing particles (photons or electrons) and increases with decreasing wavelength. Optical microscopes are thus heavily limited by the wavelength of visible light whereas the wavelength of electrons in a SEM can be orders of magnitudes smaller than for visible light. SEM therefore enables imaging of structures that are significantly smaller than the wavelength of visible light.

The electrons in a modern SEM are usually generated by a field emission gun in which they are extracted from a small tip using an electric field. The electrons are then accelerated through a column by voltages of up to 30 kV where higher voltages gives higher energy and thus smaller wavelength. The beam of electrons then passes through a series of apertures and magnetic lenses where the beam size and focus is controlled. Due to both magnetic and electric forces, the electrons spiral down in a helical trajectory along the optic axis of the lens system. The focused electron beam is then scanned point by point in a rectangular pattern on the sample surface creating a digital image pixel by pixel. Different detectors detect different signals such as back scattered electrons or secondary electrons. When

investigating surfaces, secondary electrons gives the most information. Secondary electrons are generated close to the surface and are sensitive to material and structural differences. These low energy electrons are detected by a secondary electron detector which collects the electrons using a small positive bias. The image is thus constructed from the number of collected secondary electrons at each position as the beam is scanned across the surface. This very different from how images are formed in optical microscopy where the entire image is obtained at once.

2.3.1 Focused ion beam

The focused ion beam (FIB) technique works almost identical to SEM and is therefore usually combined with SEM in the same tool. As the name suggests, a beam of ions is used instead of electrons. In the tool used during this project the ion source contained gallium ions. FIB is mainly used for milling (physical etching) of material but can also be used for imaging just as with the electron beam. The ion beam will however sputter material due to the bombardment of heavy ions and is thus not ideal for imaging. FIB is therefore usually used to mill holes on the sample surface in order to image cross sections or to prepare transmission electron microscope specimens. The column in which the ions are accelerated in is usually tilted relative to the electron column (52° in the tool used during this project). Milling is then performed with the ion beam orthogonal to the surface whereas imaging with the electron beam is performed at 52° relative to the surface.

2.4 Lithography

In order to transfer a pattern to a wafer, an intermediate pattern transfer layer is needed, i.e. a mask. The reason for this is because many processes are performed on entire wafers and are difficult to perform locally, such as etching and epitaxial growth. A patterned mask thus defines the areas of a wafer that will be exposed to a certain process whereas it protects the rest of the wafer. Such masks are created using lithography in which patterns are formed in a *resist* which is a thin film that is present on the wafer surface. This allows for patterns to be printed in the resist using methods such as exposure to light or electrons. The resulting lithography pattern can then be used as a pattern transfer layer as patterns are

transferred onto the wafer using "full wafer processes". After the wafer has been processed, the resist has served its purpose and can be removed.

2.4.1 Resists in electron beam lithography

The creation of patterns in a resist is achieved by *locally* altering the chemical properties of the resist. In electron beam lithography (EBL), this is performed by bombarding parts of the resist with electrons. As the electrons enter the resist, they gradually transfer their energy to the molecules in the resist through inelastic collisions. This transferred energy is used to break bonds between the molecules thus changing the chemical properties of the resist. The exposed areas form new materials as a result of the broken bonds and are no longer identical to the unexposed regions. The different properties between the exposed and unexposed regions of the resist is what makes pattern formation using lithography possible.

2.4.2 Spin coating of resists

Resists for EBL are usually refereed to as e-beam resists (electron beam resists). An e-beam resist is a chemical solution that is spin coated from liquid form into a thin film on wafers prior to patterning. Spin coating is a technique where the resist liquid is applied to the surface of the wafer after which the wafer is rotated at high angular speeds. The centrifugal force will spread the resist across the entire wafer until a thin film remains. The thickness of the coated film is determined by the spinning speed, spinning time, viscosity of the liquid, and the dilution. Resists are sometimes diluted with solvents in order to control the final thickness.

2.4.3 HSQ e-beam resist

There are several kinds of e-beam resists that have different properties depending on the application of the final pattern. Two examples of common e-beam resists are polymethyl methacrylate (PMMA) and hydrogen silsesquioxane (HSQ). The HSQ which was used throughout this project is a negative inorganic resist with chemical formula $[HSiO_{3/2}]_n$. Unlike PMMA, which is an organic resist, HSQ is an inorganic spin-on-glass resist which turns into SiO_2 upon exposure. This makes

HSQ a negative resist since the exposed areas of the resist make up the final pattern. In a positive resist such as PMMA, the unexposed regions make up the final pattern. Depending on the application of the pattern, a negative resist might be more convenient or vice versa.

2.4.4 EBL exposure

The exposure in EBL is performed by scanning a highly focused electron beam across the surface of a wafer coated with resist. The printed pattern is thus determined by where on the resist that the electron beam is scanned. The design in EBL is therefore a matter of telling the beam what parts of the resist to scan. This is controlled through computer software which translates user drawn patterns into coordinates on the wafer to be scanned by the beam. EBL is therefore a "mask-less" technique since it does not require a hard mask for the design as opposed to optical lithography. This is a big advantage for EBL since the design can be changed at any time with little effort.

2.4.5 Controlling the dose in EBL

The dose that the electron beam in EBL deposits into the resist is usually given as electric charge per unit area (μC/cm^2). The dose depends on the current of the beam and on the dwell time, i.e. the scanning speed of the beam. The current of the beam is controlled by apertures in the lens system and the dwell time is controlled by a pattern generator (the hardware in an EBL system is similar to the hardware in a SEM as described in section 2.3). The dwell time is defined as the time the electron beam is stationary at each position. A long dwell time thus deposits more charge into the resist and vice versa. Both the current and the dwell time must be carefully set prior to patterning in order to achieve a specific dose. The current of the beam is usually measured from which the dwell time for a specific dose is calculated. Different combinations of currents and dwell times can result in identical doses but the total time required for patterning may vary. Low currents in combination with long dwell times are more time consuming since the beam has to expose each position for a longer time. Faster patterning can be achieved by choosing higher currents and shorter dwell times. There is however

often a limit on the shortest allowable dwell time that the pattern generator can handle.

The deposited dose can be constant throughout an entire patterning process, or it can vary depending on the geometry of the design elements. This is simply solved by assigning different dwell times to the different design elements. Closely spaced design elements often require somewhat lower doses and are sensitive to variations. More spread-out elements might be able to sustain higher doses and are less sensitive to variations. The reason for this is an effect called the *proximity effect* where the incident electrons back-scatter in the resist and unintentionally expose other parts. The proximity effect is also dependent on the thickness of the resist where a thick resist gives rise to more back-scattered electrons and unintentional exposure. Exposure of design elements on a thick resist might therefore require a lower dose than for identical structures on a thinner resist. Another effect called the *forward scattering effect* might also be present which comes from electron-electron interactions in the resist. In this effect the incident electrons are deflected at small angles due to the electron density in the resist. This results in a broadening of the incident electron beam and might also lead to unintentional exposure. A thin resist with low electron density can suppress forward scattering. In addition to all the general characteristics mentioned above, the dose is heavily dependent on the resist that is used. PMMA, for example, is a low sensitivity resist and thus require considerably lower doses than HSQ. The reason for this is the lower energy required to change the molecular structure in PMMA than in HSQ. All of this must be considered when preparing the exposure in EBL.

2.4.6 Development of resists

After patterning, the excess e-beam resist that is not part of the final pattern must be removed. This is a wet process and is called *development* and is performed by immersing the wafer in a solution, called *developer*. Since the exposure alter the chemical properties of a resist, a developer can be chosen that only dissolves desired parts of the resist. For a negative resist such as HSQ, the developer only dissolves the unexposed resist. The exposed regions have been chemically transformed into SiO_2 and are not affected by the developer and will thus remain on the wafer surface. The purpose of the development process is thus to bring out the printed pattern by removing resist that is not part of the pattern. Generally, different

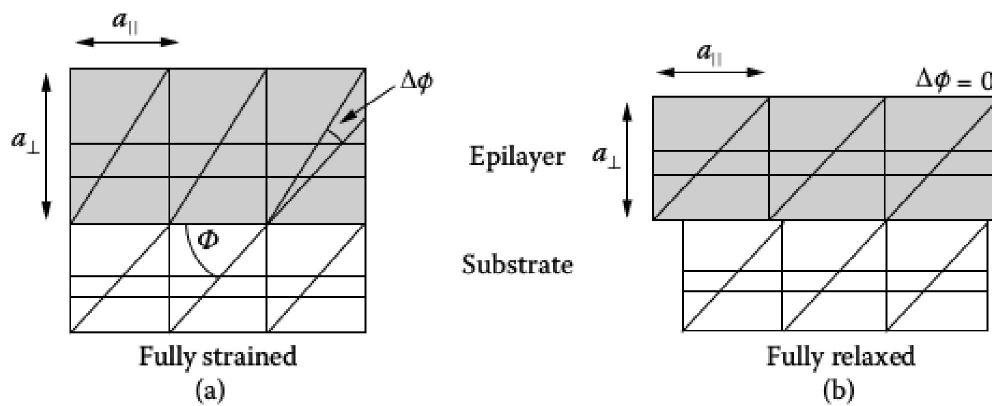

FIGURE 2.3: a) Tetragonal distortion and b) strain relaxation in epitaxial layers [18].

resists require different developers. A certain resist may however have several developers that work. They might however work differently good under various conditions. A common developer for HSQ that will be used during this project is tetramethylammonium hydroxide (TMAH).

2.5 Strain in epitaxial films

Strain arises when a crystal atomic lattice is deformed from its natural bulk state. This usually occurs during heteroepitaxial growth of thin films where the lattice constant of the film differs from that of the substrate. During growth, the unit cell of the thin film will be distorted to assume the same in-plane lattice constant as the substrate. The distortion can be either tensile or compressive depending on the actual case. Tensile strain arises when the in-plane lattice constant of the thin film is smaller than that of the substrate. The unit cell of the thin film will thus be stretched in the horizontal direction (parallel to the surface) in order to fit the substrate. Subsequently, in order to maintain a constant volume of the unit cell, the lattice of the thin film is compressed in the vertical direction (normal to the surface). There is thus a tensile strain parallel to the surface and a compressive strain in the normal direction. This is known as *tetragonal distortion* and refers to the distortion of an initially cubic unit.

Figure 2.3 a) illustrates tetragonal distortion in a fully strained epitaxial layer. It is clear that the unit cell has shrunk in the direction parallel to the substrate

and expand in the normal direction and is no longer cubic. The interplanar spacing normal to the surface as well as the angle $\Delta\phi$ of the asymmetric planes has changed. In a tetragonally distorted epitaxial layer, the angle of a set of asymmetric $\{hkl\}$ planes differs by $\Delta\phi$ from the same set of planes in the substrate. This is characteristic for tetragonally strained layers and is used to pinpoint changes in the unit cell due to strain.

If an epitaxial layer with cubic crystal structure is unstrained (not tetragonally distorted), it is said to be relaxed. This is shown in figure 2.3 b) where the epitaxial layer does not exhibit tetragonal distortion. The dimensions of the unit cell of the epitaxial layer are completely determined by bulk properties. There is also no change in angle of asymmetric $\{hkl\}$ planes between the epitaxial layer and the substrate.

The formation of relaxed epitaxial layers is associated with the relief of strain energy. The elastically constrained energy within a strained lattice can be relieved and used to form misfit dislocations. This usually occurs as the film thickness becomes larger than a certain *critical thickness*. For thicknesses larger than the critical thickness it is energetically favorable to form defects rather than to further strain the layer. The critical thickness is a unique property for each combination of epitaxial layer and substrate. It is determined by the lattice mismatch and increases with decreasing lattice mismatch. Material combinations with large lattice mismatch are therefore heavily limited in the thickness of strained epitaxial layers. A theoretical model to calculate the critical thickness of epitaxial InGaAs films grown on InP(001) is presented in appendix A.

2.6 High resolution X-ray diffraction

High resolution X-ray diffraction (HRXRD) is one of several techniques that utilize X-rays to investigate crystals [18]. It is widely used in the semiconductor industry to examine singe crystals, either bulk substrates or epitaxial films. Other techniques such as powder X-ray diffraction exist but are more suitable for other purposes, e.g. phase identification. The concept of using diffracted X-rays as information carriers is however the same for both techniques. The fundamental principle for all techniques using X-ray diffraction is that incident X-rays scatter against atoms in the crystal lattice and gives rise to diffraction. Diffracted X-rays

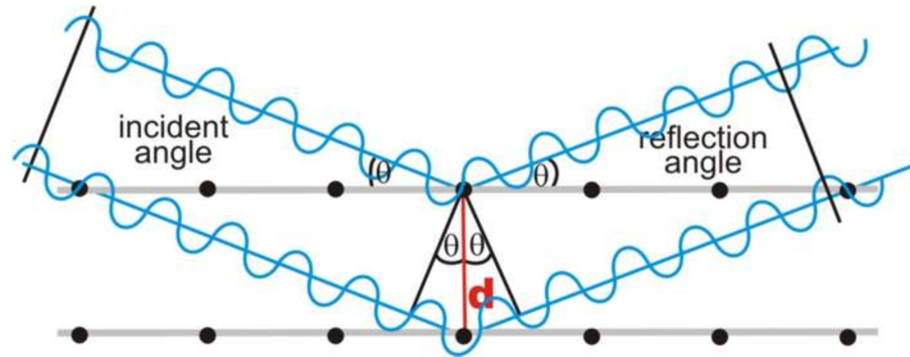

FIGURE 2.4: Illustration of Bragg's law with incident and reflected X-ray waves.

carry valuable information and can be used to calculate several important parameters related to the crystal structure. A few examples of measurable parameters that are especially interesting for semiconductors are the lattice constant, the degree of strain in thin films, the material composition in alloys, the thickness of epitaxial layers and many more.

2.6.1 Bragg's law

HRXRD relies on Bragg's law, i.e. the diffraction of short wavelength X-rays from a set of atomic planes. The X-rays are incident towards a specific set of crystal planes where they undergo reflection. The reflected X-rays then exit the crystal at the same angle as they entered it (law of specular reflection). A detector is therefore placed at the angle of specular reflection in order to detect the reflected X-rays. Followed by reflection of the X-rays, constructive interference and diffraction can occur. This only happens when Bragg's law is satisfied and is expressed as

$$n\lambda = 2d_{hkl}\sin\theta \tag{2.3}$$

where n is an integer, λ is the wavelength of the X-rays, d_{hkl} is the interplanar spacing of a set of $\{hkl\}$ planes, and θ is the angle of the X-ray beam relative to the $\{hkl\}$ planes. An illustration of Bragg's law and how X-rays interact with atomic planes is shown in figure 2.4.

During HRXRD experiments, all the variables in equation 2.3 are usually fixed except the angle of incidence. A common measurement called $2\theta-\omega$ is therefore to scan the angle of incidence and simultaneously detect the reflected X-ray intensity.

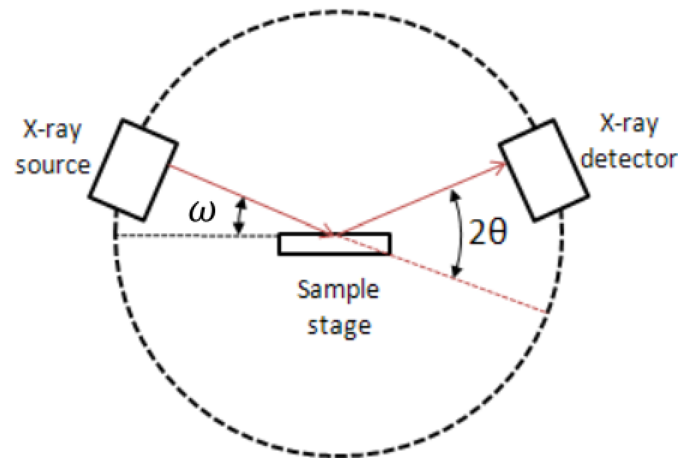

FIGURE 2.5: Illustration of the movement of sample holder and detector during a $2\theta - \omega$ HRXRD measurement.

This is done by scanning the sample relative to the X-ray beam, known as an ω scan, and at the same time scan the detector in a synchronized way around the sample, known as a 2θ scan. The geometry of the experimental setup requires the detector to move at twice the speed of the sample, hence the name $2\theta - \omega$. Figure 2.5 illustrates how the sample and detector moves in a coupled $2\theta - \omega$ scan. The X-ray source is fixed and does not move, only the sample holder and detector are allowed to move. The ω angle is defined as the angle between the reflecting atomic planes and the X-ray beam whereas the 2θ angle is the angle between the X-ray beam and the position of the detector. For a symmetric reflection, i.e. a measurement of the atomic planes that are parallel to the sample surface, the 2θ angle is always twice the ω angle. This is however not true for asymmetric reflections, i.e. reflections from planes that are inclined with respect to the sample surface. Measurements of asymmetric reflections are usually carried out in grazing incidence or grazing exit geometries where the beam either enters or exits the sample at very small angles. To clarify, a symmetric reflection would be the (111) reflection from a (111) wafer, or equally the (220) reflection from a (110) wafer. Similarly, the (531) reflection would be an asymmetric reflection for both of the wafers since neither of them have (531) planes parallel to the surface.

2.6.2 Diffraction in reciprocal space

In X-ray crystallography the reciprocal space is a helpful and necessary tool. It significantly simplifies the relationship between X-rays and crystal structures by assuming the inverse of length as the ”standard unit” for vectors. The reciprocal space is thus a practicality constructed with the purpose to simplify the interpretation and analysis of experimental diffraction data. As will be shown later, reciprocal space mapping (RSM) is a technique that clearly demonstrates the advantage of working in reciprocal space.

The reciprocal space is a three dimensional lattice where the lattice points are reflections from different sets of atomic $\{hkl\}$ planes. Each reflection has a reciprocal lattice vector $\vec{S}_{hkl}$ assigned to it that starts at the origin and ends at the corresponding lattice point. The magnitude and direction of $\vec{S}_{hkl}$ in reciprocal space gives information about the interplanar spacing d_{hkl} and the orientation of the $\{hkl\}$ planes. Each reciprocal lattice vector $\vec{S}_{hkl}$ is related to the corresponding $\{hkl\}$ planes according to

$$\|\vec{S}_{hkl}\| = \frac{1}{d_{hkl}} \qquad \vec{S}_{hkl} \perp \{hkl\} \tag{2.4}$$

In counterpart to Bragg's law in real space, the Laue equations describes diffraction in reciprocal space [18]. The incident and reflected X-rays are described as vectors, $\vec{k}_i$ and $\vec{k}_f$ respectively. Their magnitude is equal since the scattering is elastic, i.e. there is no energy exchange between the X-rays and the crystal lattice. A third vector called the scattering vector $\vec{Q}_{hkl}$ can be constructed by taking the difference between $\vec{k}_f$ and $\vec{k}_i$. $\vec{Q}_{hkl}$ represents the difference in momentum between the reflected and incident X-rays and has the same unit as the reciprocal lattice vectors $\vec{S}_{hkl}$. The Laue equations states that diffraction from a set of $\{hkl\}$ planes occurs when the diffraction vector $\vec{Q}_{hkl}$ equals the corresponding reciprocal lattice vector $\vec{S}_{hkl}$. Since $\vec{Q}_{hkl}$ is entirely made up by $\vec{k}_i$ and $\vec{k}_f$, which in turn are linked to λ, ω and 2θ it is fairly easy to imagine how the reciprocal space is probed when scanning the diffractometer in different ways. The scenarios in figure 2.6 illustrates how the diffraction vector $\vec{Q}_{hkl}$ can be made to coincide with a reciprocal lattice vector $\vec{S}_{hkl}$ by adjusting $\vec{k}_i$ and $\vec{k}_f$. The length and the direction of the diffraction vector $\vec{Q}_{hkl}$ can be adjusted in order to probe any accessible reciprocal lattice point for a certain crystal.

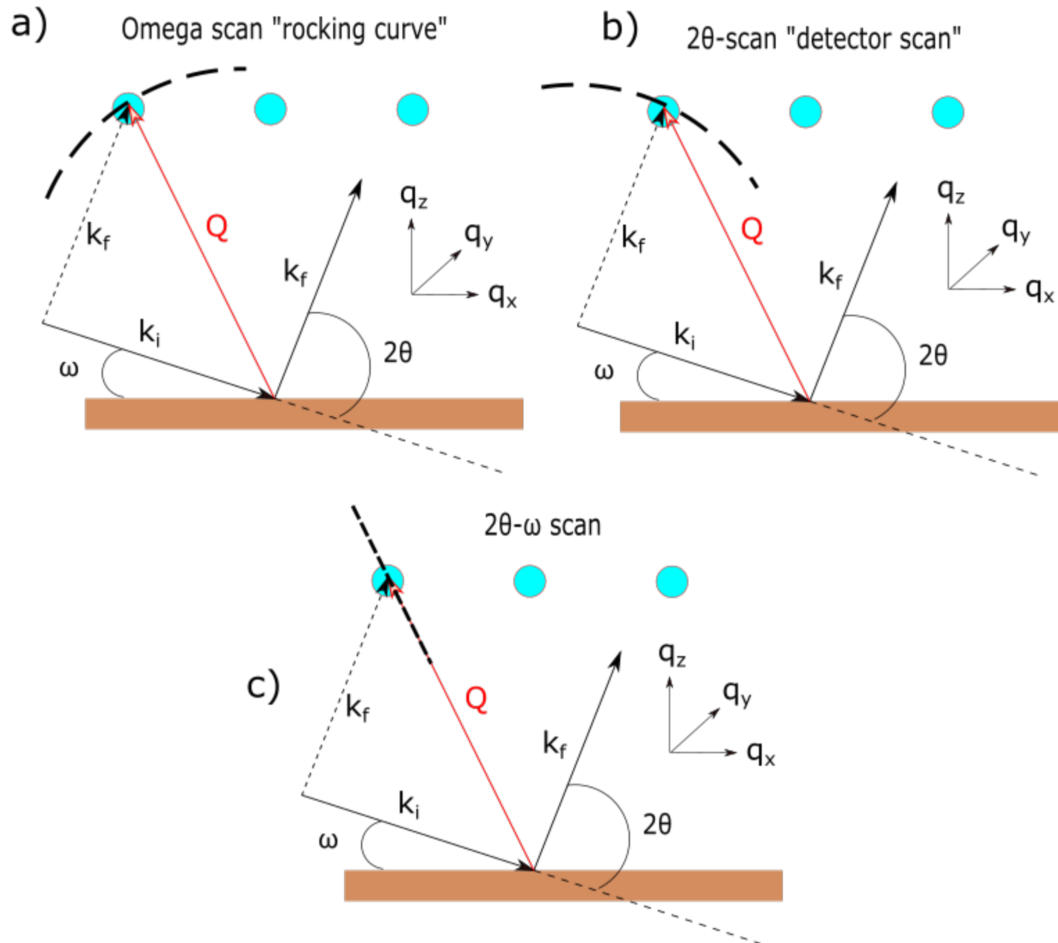

FIGURE 2.6: Illustrations of the most common ways to scan a diffractometer when investigating single crystals using HRXRD. The diffractometer is aligned to an asymmetric reflection in each of the figures.

The different scenarios in figure 2.6 illustrates how the reciprocal space is probed when the diffractometer is scanned in different ways. All of the scenarios in figure 2.6 show the initial and final wave vector $\vec{k}_i$ and $\vec{k}_f$ as well as the resulting diffraction vector $\vec{Q}$ which is aligned to an asymmetric reflection. The angles ω and 2θ are displayed in all the figures in order to simplify the demonstration of the change in $\vec{Q}$ as ω and 2θ are changed. The thick dashed line in each figure represents the path of the endpoint of $\vec{Q}$ in reciprocal space when the corresponding scan is performed. Figure 2.6 a) illustrates how the scanning of ω probes the reciprocal space where $\vec{Q}$ traces out an arc with radius $1/\lambda$ centered at the origin. In figure 2.6 b), the scanning of 2θ traces out another arc that runs along the circumference of the Ewald sphere (in a 2-dimensional cross section). In a coupled $2\theta - \omega$ scan as shown in figure 2.6 c), $\vec{Q}$ runs along a straight line through the origin and thus only the length of $\vec{Q}$ is varied.

Chapter 3

Experimental methods

3.1 Reciprocal space mapping

Reciprocal space mapping (RSM) is a technique used to map parts of the reciprocal space of crystals. It is a powerful method that offers many advantages compared to single line scans such as ω and $2\theta - \omega$ scans. RSMs are often set up to collect asymmetric reflections from substrates and films that are put together into a map. The positioning and the shape of the reflections can be used to calculate several important material related parameters. RSM is particularly useful in the determination of strain relaxation in epitaxial layers due to its ability to separate changes in the unit cell due to strain or other effects such as material composition. As discussed in section 2.5, the tetragonal distortion of an epitaxial film causes the asymmetric $\{hkl\}$ planes in the film to shift by an angle $\Delta\phi$ relative to the same set of planes in the substrate. This in turn causes the corresponding reciprocal lattice vector $\vec{S}_{hkl}$ belonging to the film to change direction since it must stay perpendicular to the asymmetric $\{hkl\}$ planes. A substrate with a tetragonally distorted epitaxial film will thus have reciprocal lattice vectors $\vec{S}_{hkl}$ from the substrate and film pointing in slightly different directions. In a relaxed epitaxial film, there is no tetragonal distortion and the reciprocal lattice vector $\vec{S}_{hkl}$ from the substrate and film will therefore be in the same direction. This means that for relaxed epitaxial films it is possible to probe asymmetric substrate and layer reflections in the same scan using a single $2\theta - \omega$ scan. This is on the other hand not be possible for substrates containing strained films.

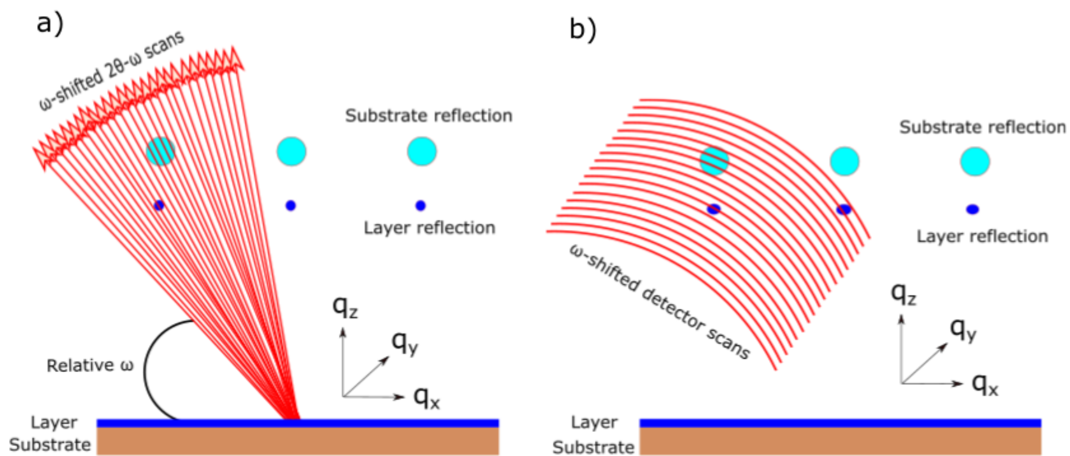

FIGURE 3.1: Illustration showing the procedure of reciprocal space mapping a) using consecutive ω-shifted $2\theta - \omega$ scans with a scintillator detector and b) ω-shifted detector scans with a PSD.

The collection of RSMs can be carried out in several ways depending on the diffractometer setup and detector type. The simplest and most common way is to collect a large series of ω-shifted $2\theta - \omega$ scans with a scintillator detector. The $2\theta - \omega$ scans are often collected in the vicinity of a known substrate reflection with the hope of capturing a reflection from the epitaxial film.

In order to span an area of the reciprocal space, the direction of the $2\theta - \omega$ scans is slightly changed between each scan as shown in figure 3.1 a). The direction of the $2\theta - \omega$ scans is controlled by changing the ω angle. Usually hundred(s) of $2\theta - \omega$ scans are collected where ω is changed over a small range, often less than a few degree(s). The end result is a 2-dimensional map with the data from the $2\theta - \omega$ scans along one axis and the ω-direction along the other axis.

For the evaluation of material composition in epitaxial films consisting of ternary III-V semiconductors, asymmetric reflections must be used during RSM. This is because there are two degrees of freedom in the dimensions of the unit cell for ternary III-V epitaxial films, namely strain *and* material composition. RSMs of asymmetric reflections gives information about the tetragonal distortion in the film which enables the strain to be calculated. The effect of strain on the unit cell must then be eliminated so that only one degree of freedom remains, that is, the material composition. It is thus not enough to just know the dimensions of the unit cell when there are two degrees of freedom. Both strain and material

composition affects the dimensions of the unit cell which is why they need to be distinguished.

3.1.1 Position sensitive detectors

Position sensitive detectors (PSD) are sometimes used to collect RSMs due to their fast data collection rate. As opposed to a scintillator point detector, a PSD can measure intensity *and* position (angle) simultaneously. An example of a PSD is a detector that consists of a 1-dimensional array of photo sensitive p-i-n junctions that each serves as individual detectors. The LynxEye detector from Bruker AXS uses this technology and consists of 192 individual detectors, covering a 2θ range of 2.7°. This enables fast collection of RSMs since the detector can measure intensity of several 2θ angles simultaneously. If the scan range in 2θ is less than or equal to 2.7°, the LynxEye does not have to move during the collection of RSMs. Usually the LynxEye does not collect ω-shifted $2\theta - \omega$ scans but rather ω-shifted detector scans. This is preferred since detector scans are collected very fast with the LynxEye. Figure 3.1 b) illustrates the concept of collecting RSMs using consecutive detector scans with a PSD.

3.2 Facet selective growth

Epitaxial growth results in layers with identical crystal orientation as the substrate. Ideally, epitaxial growth on a planar substrate results in the same planar morphology in the epitaxial layer. However, if the growth is disturbed (by a growth mask or defect) other crystal facets may form. A facet is a surface with a different crystallographic normal than that of the substrate. Facets are formed since the growth in different crystallographic directions have different growth rates. A slow-growing facet will predominantly determine the geometry of 3-dimensional structures grown on a flat surface. The growth rate of a given facet depends on the energy of an adatom on that facet. Adatoms always strive to minimize the total energy of the system and will diffuse to facets with lower surface energy. The diffusion of adatoms is characterized by the diffusion length which depends on several parameters such as temperature, substrate orientation, and source molecules. The reconstruction of a surface is therefore determined by the growth rate of a certain facet with respect to other facets within an adatom diffusion length [16].

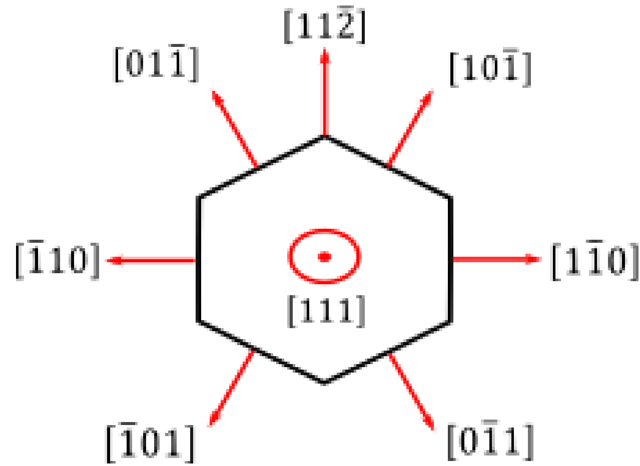

FIGURE 3.2: Illustration of the hexagonal symmetry of {110} facets on an InP(111)B substrate (seen from above the substrate).

3.2.1 Facets on InP(111)B

In the case of InP(111)B, the surface of the substrate contains cations only, i.e. phosphor atoms. This makes the growth rate on InP(111)B heavily dependent on the partial pressure of the group V precursor, i.e. AsH_3 in the case of InGaAs growth. For a specific total molar flow of the group III precursors, the group V partial pressure is controlled by the molar flow of the group V precursor. This is known as the V/III ratio and is the ratio between the molar flows of the group V and group III precursors. A high V/III ratio can therefore suppress the growth rate on an {111}B facet whereas a low V/III ratio can accelerate the growth rate.

The facets of interest in this work are equivalent {110} facets which are orthogonal to the [111]B growth direction. Figure 3.2 illustrates the hexagonal symmetry of all the possible {110} facets which are rotated 60° relative to each other. Since there are in total six equivalent {110} facets in figure 3.2, there are thus three possible orientations in which fins with vertical {110} faceted sidewalls can be grown.

3.2.2 Growth of fins using a growth mask

The epitaxial growth of structures such as fins require a growth mask present on the substrate during growth. The purpose of the growth mask in this work is to force the formation of {110} facets. An example of a growth mask suitable for this

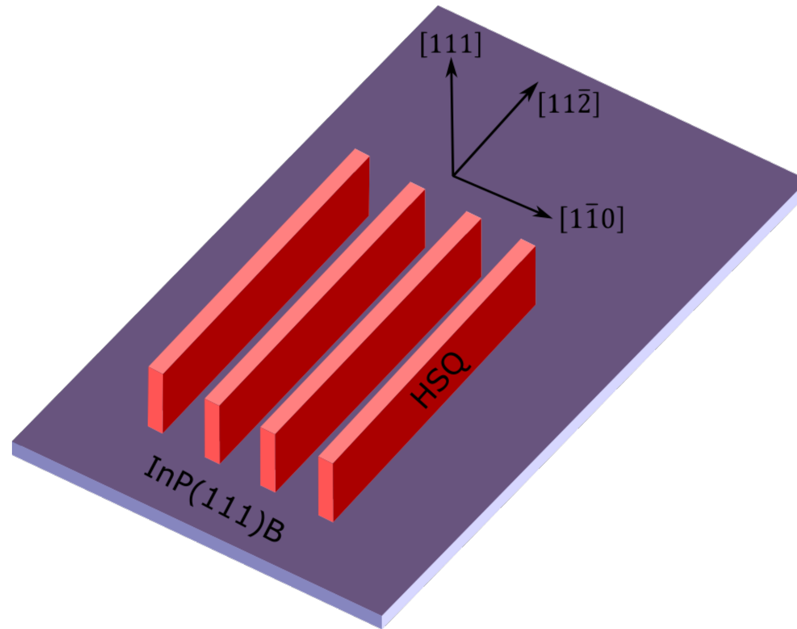

FIGURE 3.3: Illustration of a growth mask consisting of HSQ lines aligned to [11$\bar{2}$] and with sidewalls in the [1$\bar{1}$0] direction.

work is shown in figure 3.3 where HSQ lines have been patterned on the substrate using EBL. In order for the growth mask to work, the HSQ lines must be oriented in the correct direction on the substrate. This is the case in figure 3.3 where the HSQ lines are aligned to the [11$\bar{2}$] direction such that the sidewalls are oriented towards the [1$\bar{1}$0] direction. Equivalently due to the hexagonal symmetry of the {110} facets, the HSQ lines in figure 3.3 can be rotated in integers of 60° and still produce {110} facets.

Chapter 4

Results and discussion

4.1 Epitaxial growth calibration of InGaAs films

Epitaxial growth of thin InGaAs films was performed to calibrate the growth conditions prior to the formation of InGaAs fins. This was done by growth of thin InGaAs films on InP(111)B, InP(110), and InP(001) substrates. Certain growth parameters such as the gas phase composition and the V/III ratio were systematically varied in order to obtain InGaAs films with different chemical compositions. The aim of this calibration step was to obtain an understanding of the growth of InGaAs films on different InP substrates.

The epitaxial growth of undoped InGaAs films on InP substrates was realized by MOVPE in a horizontal reactor. The InP substrates were cut from semi insulating iron doped InP(111)B, InP(110), and InP(001) wafers. Several substrate pieces from different wafers were placed in the reactor simultaneously in order to ensure identical growth conditions. The growth temperature was set to 600°C and the precursors used for the group III and V elements were TMIn and TMGa, and AsH_3 respectively. The purpose of growing at 600°C is connected to the characteristics of the growth rates in MOVPE. If the chemical reaction rates at the surface limit the overall growth rate, an increased temperature may lead to faster growth rate given that the supply of precursors to the surface is fast enough. If the supply of precursors to the growth surface is slower than the chemical reaction rates, a higher temperature will not generate faster growth rate. Epitaxial growth of InGaAs can therefore be performed at a range of temperatures depending on the choice of precursors and desired growth rate. For sake of comparison reasons, the

Table 4.1: Parameters for the growth of InGaAs films on InP(001) and InP(111)B.

Batch #	TMGa flow [μmol/min]	TMIn flow [μmol/min]	Total group III flow [μmol/min]	AsH_3 flow [μmol/min]	Gas phase comp. [%]	V/III [a.u.]
A	39.8	29.9	69.7	2230	42.9	32
B	47.8	24.3	72	2230	33.7	31
C	58.1	19.1	77.2	2230	24.7	28.9
D	63.7	15	78.7	2230	19.0	28.3

thin films were grown at 600°C since the future InGaAs fins were planned to be grown at the same temperature.

The samples that were grown for composition evaluation are presented in table 4.1 together with their corresponding growth parameters. To each batch A, B, C and D belongs one InP(001) substrate and one InP(111)B substrate. The goal was to grow InGaAs layers with varying composition under identical conditions on InP(001) and InP(111)B substrates. This was done by adjusting the ratio of the molar flows of the group III precursors between each batch. The molar flows were calculated using equation 2.1 and 2.2 together with the flow of the injected H_2 carrier gas into each bubbler. The temperature of the bubblers containing TMGa and TMIn was set to 10°C and 17°C respectively. The reason for this is the high volatility of TMGa compared to TMIn. The vapor pressure of TMGa is approximately a factor 100 bigger than for TMIn at the temperatures specified above. An equal flow of H_2 carrier gas into each bubbler would thus result in a significantly higher molar flow of TMGa than for TMIn. During growth, the flow of the H_2 carrier gas that goes into the TMGa bubbler is therefore much smaller than the flow that goes into the TMIn bubbler. The total molar flow of the group III precursors and the molar flow of the AsH_3 was held approximately constant in order to achieve a constant ratio between the group V and group III precursors (called V/III ratio). The gas phase composition is defined as the ratio between the molar flow of TMIn and TMGa as they enter the reactor in the gas phase.

4.2 Reciprocal space mapping and composition evaluation

Reciprocal space maps (RSMs) of all batches presented in table 4.1 were collected in order to evaluate the composition of the epitaxial InGaAs films. The maps were collected in grazing incidence geometry using (224) and (531) reflections for the (001) and (111)B substrates respectively. Both of these reflections are asymmetric reflections which, as discussed in section 2.5 and 3.1 is nessecary if the composition and the strain is to be measured in a ternary compound semiconductor.

The chemical composition x of $In_xGa_{1-x}As$ can be calculated from Vegard's law which relates the chemical composition of a ternary semiconductor to the lattice constants of its binary constituents [11]. In the case of InGaAs, the lattice constant is assumed to be an interpolation between the lattice constants of GaAs and InAs. According to Vegard's law, $In_xGa_{1-x}As$ can thus have a lattice constant in the range of $a_{GaAs} < a_{InGaAs} < a_{InAs}$ depending on the chemical composition x.

In order to apply Vegard's law to InGaAs, the lattice constant of InGaAs in its natural (bulk) state must be known. By measuring the lattice constant of an epitaxial InGaAs film where the lattice is potentially strained may therefore not directly give the correct composition with Vegard's law. Additional calculations or measurements must be performed in order to eliminate the effect of strain on the lattice constant. A possible solution for this is RSM which has the ability to distinguish between strain and composition related effects. A RSM makes it possible to, from a strained epitaxial layer, calculate the lattice constant of a film as if it would be un-strained. The un-strained lattice constant then gives the correct composition with Vegard's law. This is usually performed by software by fitting experimental data to simulated data.

4.2.1 InGaAs films on InP(111)B

Figure 4.1 shows a complete set of RSMs for InGaAs films grown on InP(111)B according to the batches in table 4.1. The maps in the figure are labeled accordingly with respect to table 4.1 where map a) corresponds to batch A and so on. The most intense (red) peaks in all the figures in figure 4.1 corresponds to the reflection from the substrate whereas the second most intense peaks comes from

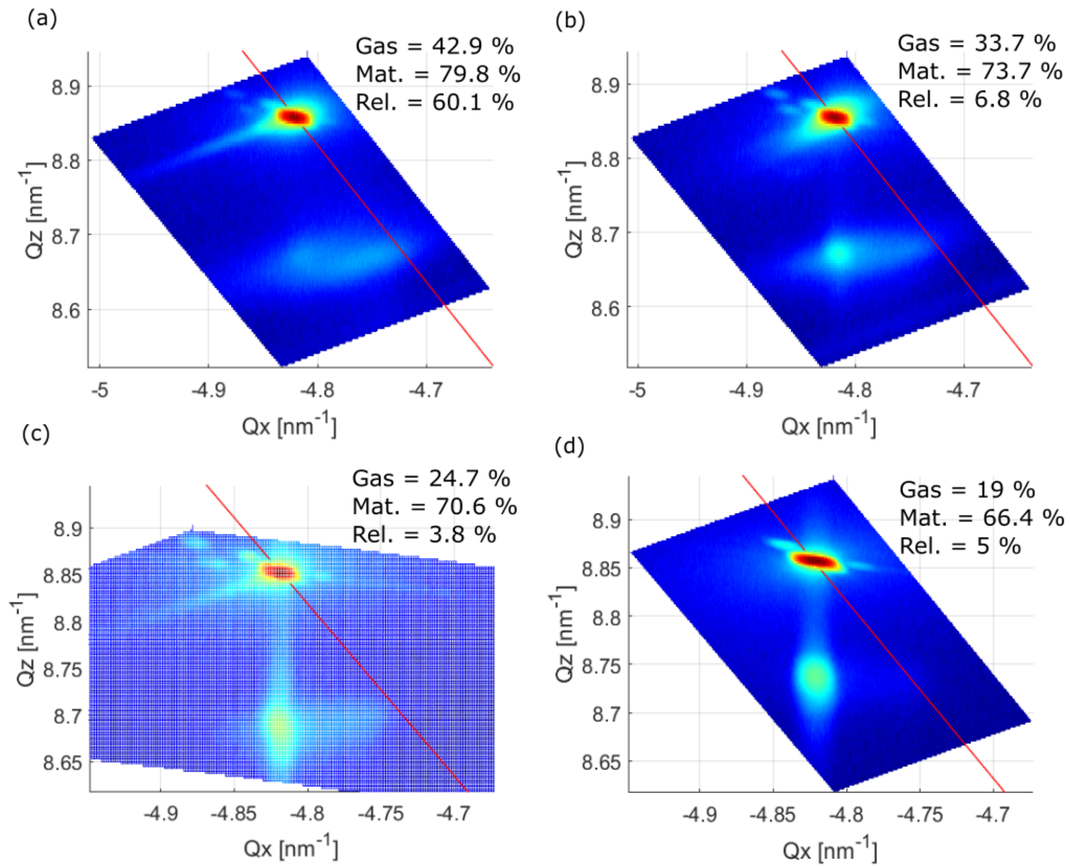

FIGURE 4.1: RSMs near the asymmetric (531) reflection of InGaAs layers on InP(111)B substrates. The maps are labeled accordingly with respect to the batches in table 4.1.

the InGaAs layer. The rectangular shape of maps a), b) and d) is a result of the consecutive ω-shifted $2\theta - \omega$ scans that were used to collect the maps using a scintillator detector. Map c) was collected using a position sensitive detector (PSD) and thus has a different shape. The PSD collects consecutive ω-shifted detector scans which yields a similar map but much faster. The total data collection time was reduced from 18 to 3 hours by using the PSD instead of the scintillator detector.

The red line included in all the maps in figure 4.1 is called the *relaxation line*. The relaxation line is a straight line that starts at the origin of reciprocal space and runs towards the substrate reflection. It represents a single $2\theta - \omega$ scan and is the line on which the reflections from a fully relaxed epitaxial layer would lie on. In a fully relaxed epitaxial layer the tilt $\Delta\phi$ of the asymmetric planes has disappeared due to strain relief. A layer reflection on the relaxation line thus implies that the direction of the asymmetric planes in the layer is in the same direction as for

TABLE 4.2: Comparison of gas phase composition and material composition in epitaxial $In_xGa_{1-x}As$ layers on InP(111)B.

Batch	Gas phase comp. [%]	Material comp. [%]	Relaxation [%]
A	42.9	79.8	60.1
B	33.7	73.7	6.8
C	24.7	70.6	3.8
D	19.0	66.4	5.0

the substrate and no tetragonal distortion in the layer is present. Also note the difference in how the relaxation line runs in maps collected with the scintillator detector and the PSD, e.g. the difference between figure 4.1 c) and d). Since maps collected with the scintillator detector consists of a series of $2\theta - \omega$ scans, the relaxation line which represents a single $2\theta - \omega$ scan, runs in the same direction as the scans in the map (parallel to the long side of the map in figure 4.1 a), b) and d)). On the other hand, the consecutive detector scans collected by the PSD are not straight lines that runs through the origin (as shown in figure 2.6 b)). The relaxation line therefore does not necessarily run parallel to any of the sides in a map collected by detector scans. This is important to keep in mind since most reciprocal space maps only cover a small part around a certain reciprocal lattice point. The direction in which the origin is located in may not always be obvious. Displaying the relaxation line therefore helps to keep track of the directions.

The composition of the InGaAs layers were calculated using software (Leptos) supplied from the manufacturer (Bruker AXS) of the diffractometer. A virtual sample that consisted of an InP(111) substrate and an InGaAs epitaxial layer with unknown composition was created in Leptos. The virtual sample was then compared to the map and the composition of the InGaAs layer could be estimated along with the relaxation of the lattice. The estimation tool required two things in order to calculate the parameters; a map of an asymmetric reflection from a known sample (including substrate and layer peaks), and a virtual sample. All the maps in figure 4.1 were evaluated using Leptos. The results of the measured material compositions are presented in table 4.2 along with the degree of relaxation.

It can be seen that none of the most intense parts of the layer peaks in figure 4.1 b), c) and d) are located on the relaxation line. This agrees well with the results of the relaxation in table 4.2 since the degree of relaxation for these layers is rather small. There is however a small amount of intensity from the layer peaks that is smeared out towards the relaxation lines in those maps. This means that the

epitaxial InGaAs layer is partly relaxed but still mostly strained since the majority of the intensity is located away from the relaxation line. The layer peak in figure 4.1 a) is on the other hand heavily smeared out all the way to the relaxation line and has no clear spot were the majority of the intensity is located. The uniform smearing of the peak suggests that the InGaAs layer is relaxed in many different stages. Certain parts of the lattice are fully strained whereas other parts are partly or fully relaxed. This also agrees with the degree of relaxation for the batch A sample in table 4.2 which reads 60.1 %. It should nevertheless be noted that this number is the least accurate since there is no clear intensity maximum in the layer peak in map a). This complicates the fitting process since the intensity peaks must be manually specified in order to initiate the fitting. The location of the layer peak can thus be anywhere within the smeared region which gives rise to fluctuations mainly in the relaxation but also in the composition. Attempts to manually specify the layer peak at various locations within the smeared region revealed that the relaxation could be as low as 14 % and as high at 88 %. The variation in composition was significantly smaller and was always within the range of 75-82 %. The values that were chosen to be presented in in table 4.2 for the batch A sample are the ones that correspond to an intensity maximum somewhere in the middle of the smeared layer peak. It perhaps makes little sense to talk about the absolute degree of relaxation in layers that are as relaxed as the one in map a) since they seem to suffer from varying relaxation and composition throughout the lattice.

4.2.2 InGaAs films on InP(001)

The growth of InGaAs layers on InP(001) was performed under identical conditions as for the growth on InP(111)B. The batches in table 4.1 therefore also represent the growth conditions under which the InGaAs layers on InP(001) were grown. Note that the batch D sample is not included for InP(001) since no layer reflections, symmetric nor asymmetric, were visible during RSM. It is possible that the batch D sample was mixed up with a similar looking InP(001) sample with no InGaAs film on it. Figure 4.2 therefore only show three RSMs of samples grown according to batch A, B and C. The maps are again labeled accordingly so that map a) represents batch A and so on. All of the maps in figure 4.2 were recorded with the PSD since the data collection rate was much faster.

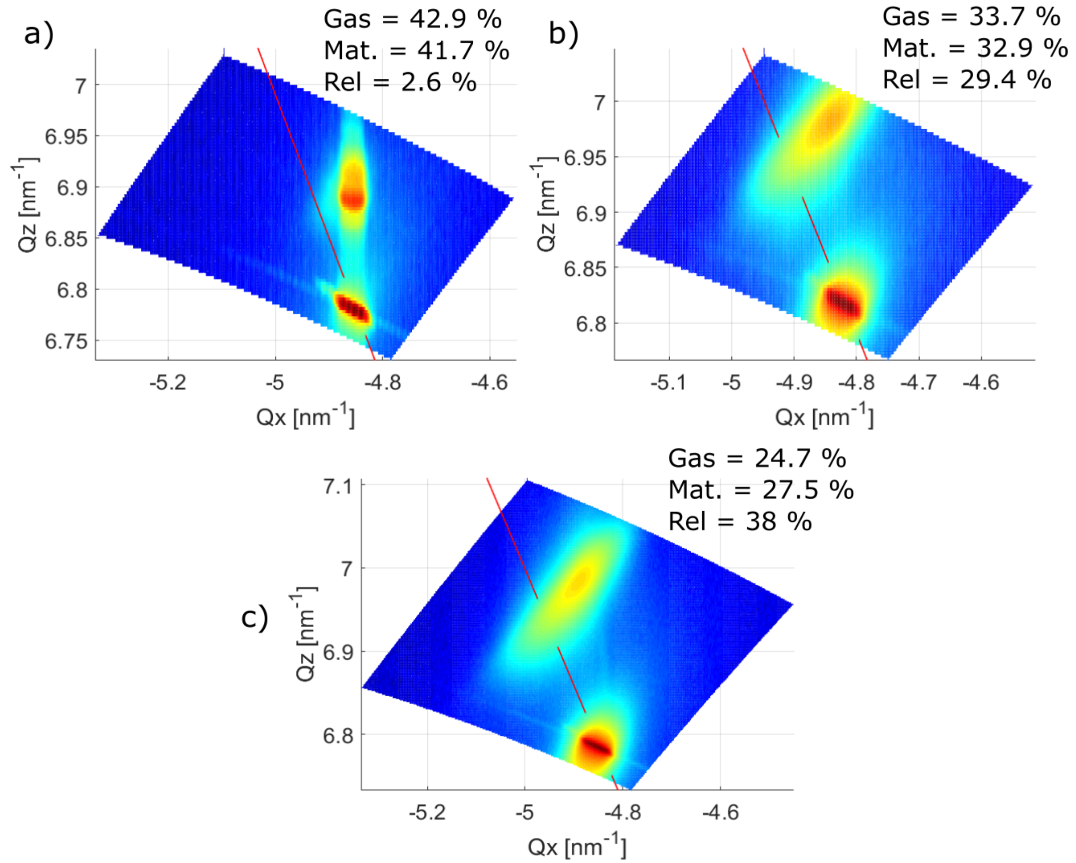

FIGURE 4.2: RSMs near the asymmetric (224) reflection of InGaAs layers on InP(001) substrates. The maps are labeled accordingly with respect to the batches in table 4.1.

The relaxation line is also present in all of the maps showing the direction of the origin. Note that in the maps from the InP(111)B samples in figure 4.1, the layer reflections are located beneath the substrate reflection whereas they are located above the substrate reflection in figure 4.2. This is a result of the $In_xGa_{1-x}As$ material composition and indicates that the InGaAs layers are gallium rich as opposed to the layers grown on InP(111)B. Table 4.3 which contains the measured compositions and relaxations confirms this, all of the layers contain more GaAs than InAs. Table 4.3 also reveals that the relaxation for the batch A sample is small whereas is it considerably bigger for the batch B and C samples. This can be verified by the position of the layer reflections in the corresponding map in figure 4.2. The layer reflections in maps b) and c) are smeared out towards the relaxation line whereas the layer reflection in map a) is not. A possible explanation for this is the lattice mismatch as discussed in section 2.5 which in this case depends on the composition of the InGaAs layers. The lattice mismatch is zero for InGaAs layers with compositions of 53 % and increases for compositions further away

Table 4.3: Comparison of gas phase composition and material composition in epitaxial $In_xGa_{1-x}As$ layers on InP(001).

Batch	Gas phase comp. [%]	Material comp. [%]	Relaxation [%]
A	42.9	41.7	2.6
B	33.7	32.9	29.4
C	24.7	27.5	38.0
D	19.0	-	-

from this. The composition of the batch A sample is closer to 53% and should be better lattice matched than the batch B and C samples. This also applies to the InGaAs layers grown on InP(111)B where the layers with compositions closer to 53% appear to be less relaxed.

4.2.3 InGaAs films on InP(110)

Few good RSMs of InGaAs films grown on InP(110) were obtained. The asymmetric layer reflections from some of the samples could not be found and others were weak and barely visible. In the end, the data was too inconsistent and was therefore chosen not to be included in the same way as for the InP(111)B and InP(001) samples.

The InGaAs films grown at 600°C on InP(110) were suspected to suffer from relaxation and was supported by ordinary $2\theta - \omega$ scans of symmetric reflections. The most intense peaks in a $2\theta - \omega$ scan represent substrate reflections whereas other peaks represent layer reflections. Sharp layer peaks indicate good crystal quality whereas broad peaks indicate relaxation. Figure 4.3 a) and b) show symmetric $2\theta - \omega$ scans from InGaAs films grown on InP(111)B and InP(110) respectively. The V/III ratio was held constant at 32 whereas the gas phase composition was varied as stated in the figures. It can be seen that the sharpness of the layer peaks in figure 4.3 a) and b) differ considerably. Two of the layer peaks in figure b) are rather broad which indicate partly relaxed InGaAs films. No clear layer peak is observed in figure b) for the film grown with a gas phase composition of 33.7 %. On the contrary, only one of the films in figure a) show signs of relaxation while the other two are of good crystal quality. Additionally, there are visible interference fringes on two of the InGaAs films grown on InP(111)B whereas there are none on the InGaAs films grown on InP(110). These observations suggest that the crystal quality of the InGaAs films grown on InP(110) is in general very poor compared to

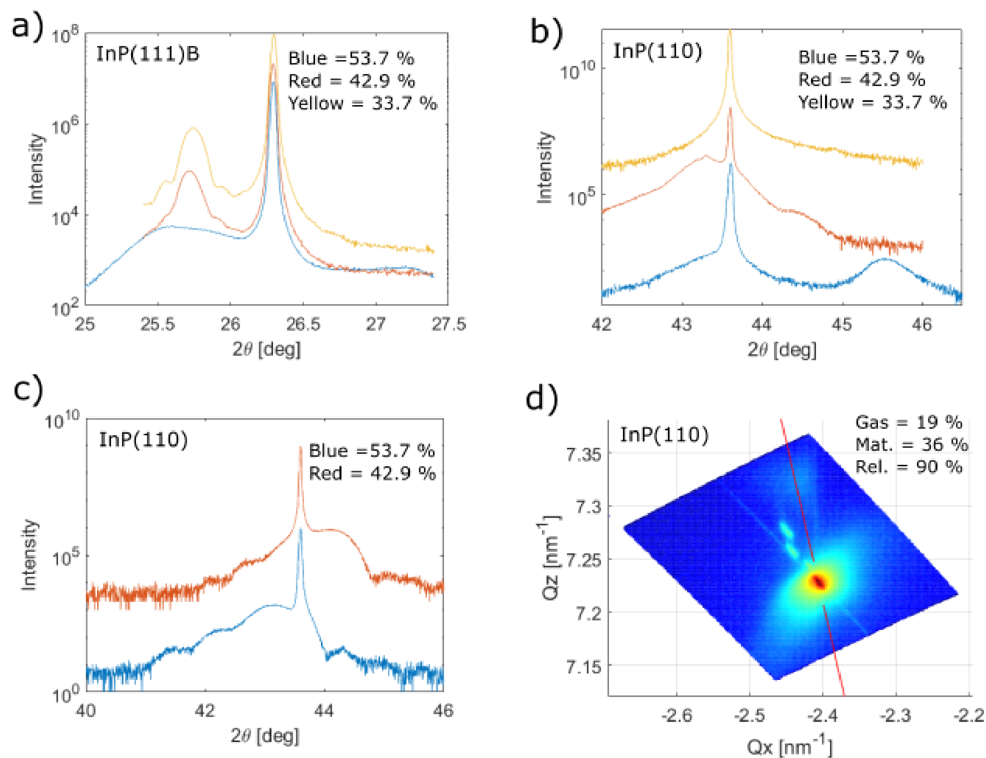

FIGURE 4.3: Figure a) and b) show symmetric $2\theta - \omega$ scans of InGaAs films grown at 600°C on InP(111)B and InP(110) respectively at a V/III ratio of 32. Figure c) show symmetric $2\theta - \omega$ scans of InGaAs films grown at 500°C on InP(110) at a V/III ratio of 32. The text included in figure a), b) and c) represent the gas phase compositions. Figure d) show a RSM of an InGaAs film grow at 600°C at a V/III of 9.

the films grown on InP(111)B. From this it is apparent that the growth conditions that resulted in good crystal quality of InGaAs films on InP(111)B and InP(001) do not work for InP(110). The reason for this is unknown and it may be related to any or all of the growth parameters. It is also possible that the InP(110) wafer was defective, damaged, or contaminated. This is however unlikely since the wafer was delivered directly from the factory. Another reason might be related to the excessive formation of defects causing the InGaAs films on InP(110) to quickly relax. A large lattice mismatch between the film and substrate would force the critical thickness to rapidly decrease and thus form defects early in the growth process. This could potentially explain why the InGaAs film grown with a gas phase composition of 53.7% in figure b) appears to be relaxed since the layer peak is located far from the substrate peak. It would however not explain the InGaAs film grown with a gas phase composition of 42.9 % since the layer peak is located closer to the substrate peak. It is therefore difficult to conclude why the InGaAs

films grown at 600°C on InP(110) turned out as they did.

The only good RSM of an InGaAs film grown on InP(110) is shown in figure 4.3 d). This film was grown with a gas phase composition of 19% at a V/III ratio of 9. It is thus not possible to compare this map to the films presented in figure b) since both the gas phase composition and the V/III ratio differs. It can be seen that the InGaAs layer reflection in figure d) is very weak and is located on the relaxation line above the substrate reflection. The material composition and the degree of relaxation was estimated to be 36% and 90 % respectively. The weak intensity from the layer reflection together with the high degree of relaxation indicates poor crystal quality of the film. The used growth conditions are therefore not optimal for growth on InP(110).

At last, two InGaAs films whose symmetric $2\theta - \omega$ scans are shown in figure 4.3 c) were grown on InP(110) at 500°C. The gas phase compositions and the V/III ratios were identical to the films grown at 600°C as presented in figure b). The growth time of the films grown at 500°C was however reduced making the films thinner which complicates the comparison to figure b). It can although be seen in figure c) that the location of the layer peaks are consistent with the gas phase compositions. There are also visible interference fringes in figure c) indicating good crystal quality of the films. According to figure b) and c), the films grown at 500°C seems to have better crystal quality than those grown at 600°C. It is thus possible that the epitaxial growth on InP(110) works better at 500°C than at 600°C. It is also possible that the reduced growth time of the films grown at 500°C led to thin defect-free films and that the reduced temperature did not matter. All of these explanations are of course only speculations since no final conclusion can be drawn due to the many degrees of freedom.

4.2.4 Comparison of growth behaviors on InP

The three previous sections have shown that epitaxial InGaAs films grown under identical conditions on InP(111)B, InP(110), and InP(001) are of different quality and have different material compositions. Figure 4.4 demonstrates the data from table 4.2 and 4.3 as a plot of $In_xGa_{1-x}As$ material composition versus gas phase composition.

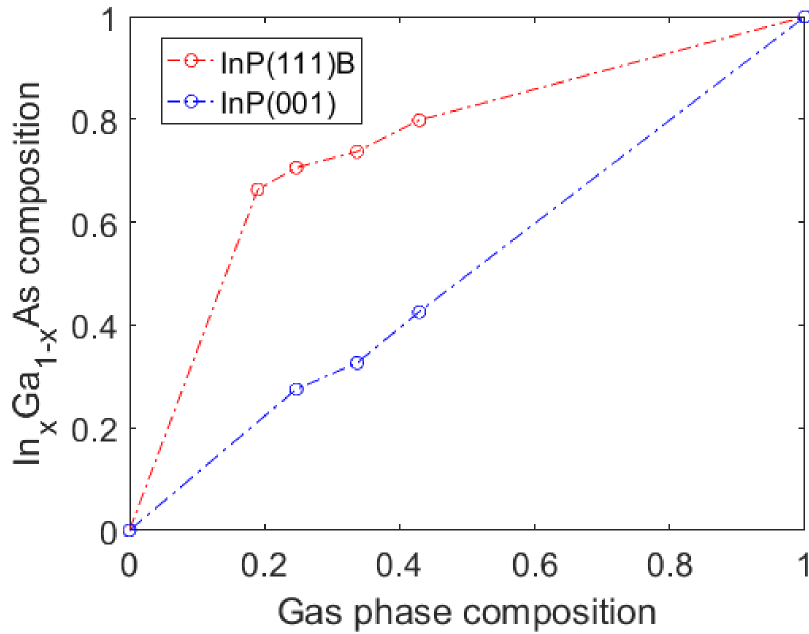

FIGURE 4.4: $In_xGa_{1-x}As$ material composition x versus the gas phase composition of the group III precursors for growth on InP(111)B and (001).

Boundary conditions were included in the plot such that gas phase compositions of 0 and 1 results in pure GaAs and InAs respectively. It can be seen in figure 4.4 that InGaAs layers grown on InP(111)B substrates tend to incorporate large fractions of InAs whereas the growth on InP(001) substrates tend to agree quite good with the gas phase composition as can be seen in the linear relationship. The growth on (111)B seems to follow a non-linear relationship where the growth of InAs is more favorable than GaAs. It is thus apparent that growth on different surfaces behave differently. This was also shown for the growth on InP(110) where the effect was even more apparent. It was found that identical growth conditions could be used to obtain InGaAs films of good quality on InP(111)B and InP(001) whereas InGaAs films grown on InP(110) were of considerably worse quality. The underlying reasons for these observations are unknown but it evidently shows that not only the substrate material matters, but also the surface. This is for example important to consider during facet selective growth where different facets grow during equal conditions and is of particular interest further in this thesis since the InGaAs fins will have sidewalls consisting of {110} facets. It is therefore important to be aware of the behavior of the formed {110} facets as the fins grow in the [111]B direction. The results have shown that the crystal quality as well as the chemical composition differed considerably between growth on InP(111)B and InP(110) during identical conditions. It is thus possible that during growth of InGaAs fins,

the chemical composition and crystal quality will be different on the {110} faceted sidewalls compared to the {111}B faceted top. According to what the results have shown, the InGaAs growth on {111}B facets would be indium rich whereas the growth on {110} facets would result in InGaAs compositions with poor lattice match and thus reduced crystal quality. The distribution of misfit dislocations inside the InGaAs due to strain relaxation could therefore potentially be shifted towards the {110} faceted sidewalls.

4.3 Preparation of the growth mask

Prior to the epitaxial growth of InGaAs fins, each InP(111)B substrate was patterned with a growth mask. The growth mask consisted of equally spaced HSQ lines arranged in arrays that were patterned in different orientations on the substrate surface. The width and the spacing of the lines was set to 50 nm whereas the length was set to 2 μm. The requirement of the growth mask was to have lines in different orientations that were correctly exposed and clean from resist residues and organic contamination. This was achieved by optimizing the exposure dose, development process, and cleaning procedure prior to the growth as described in Appendix B. Figure 4.5 shows the final result of the optimization process where the HSQ lines are correctly exposed and free from contamination.

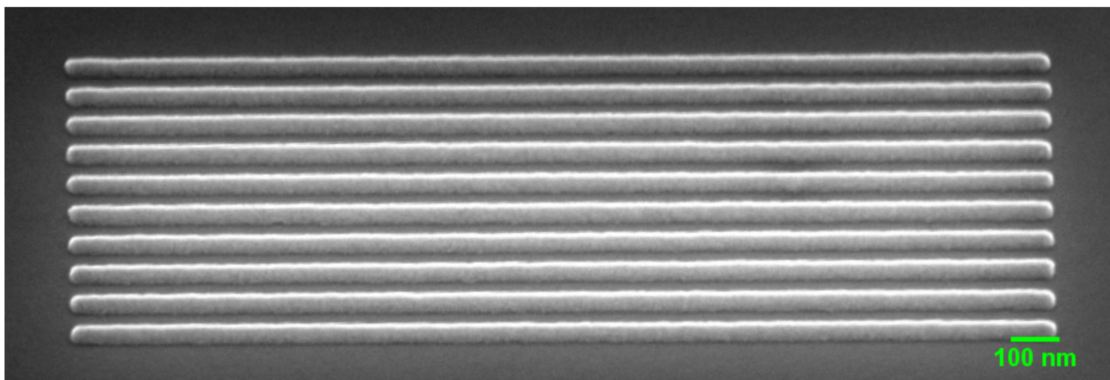

FIGURE 4.5: Scanning electron micrograph of an array of lithography patterned HSQ lines that was used as growth mask. The image is taken with the sample at 52° relative to the electron beam.

4.4 Facet selective growth of InGaAs fins

The epitaxial growth of InGaAs fins was realized by LP-MOVPE at 600°C using TMIn, TMGa and AsH_3, identical to the previous growth of thin InGaAs films. All InGaAs fins were grown with identical gas phase compositions, namely $In_{0.19}Ga_{0.81}As$. This specific composition was chosen since it produced highly strained thin $In_{0.66}Ga_{0.34}As$ films on InP(111)B as shown in table 4.2 and figure 4.1 d). The growth of those thin films was although performed at a V/III ratio of 28.3 whereas the growth of InGaAs fins will be performed at substantially lower V/III ratios. The chemical composition is however not expected to dramatically change as the V/III ratio is reduced. It is also clear that $In_{0.66}Ga_{0.34}As$ is not perfectly lattice matched to InP. Therefore, depending on the height of the grown InGaAs fins, the critical thickness might not be reached.

Several samples containing growth masks were exposed to epitaxial InGaAs growth with various input V/III ratios ranging from 5 to 30. The purpose of varying the V/III ratio was to fabricate InGaAs fins whose properties such as width, facets, and height could be investigated. As mentioned earlier, low V/III ratios were expected to accelerate the growth rate in the [111]B direction due to the low AsH_3 partial pressure in the gas phase. The growth rate in the [111]B direction relative to the [110] directions thus determine the lateral overgrowth of the mask.

4.4.1 Impact of growth mask orientation

Regarding the arrangement of HSQ lines in the growth mask, it can been seen in figure 4.6 a) that only HSQ lines in certain orientations give rise to fins with sharp profiles. The angles in figure 4.6 a) represent the angles of the HSQ arrays relative to the cleavage plane of the substrate. It can be seen in figure 4.6 a) that the HSQ lines rotated near 60° (second row) form good InGaAs fins while the other directions do not (first and third row). This is confirmed from both the sharp geometrical profile and the high contrast of the fins at 60, 61, and 62°. The sharp profile suggests that {110} facets have been formed whereas the high contrast indicates that the height of the fins exceed the thickness of the surrounding InGaAs layer. Neither of this is seen for the fins around 50 or 70° which indicates that the HSQ lines are improperly aligned in order to form {110} facets. Those fins show considerably more growth on the sidewalls and are also grown together

at certain locations as seen in figure 4.6 a). The contrast also differs from the correctly aligned fins which implies that the height of the misaligned fins is much smaller.

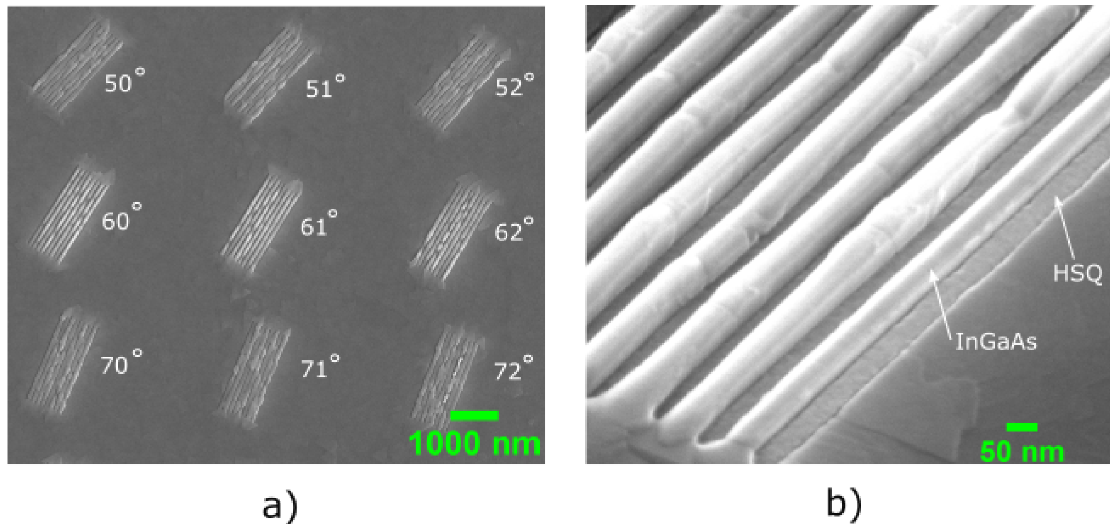

FIGURE 4.6: Scanning electron micrographs of a) arrays of fins in different orientations and b) array of fins in one of the correct orientations.

The array of InGaAs fins shown in figure 4.6 b) was grown at a V/III ratio of 5 and the image is taken from an array of correctly aligned HSQ lines. Both the HSQ lines and the epitaxially grown InGaAs fins are visible and are indicated by the corresponding arrows. It is evident that the InGaAs fins have grown higher than the growth mask and that smooth sidewalls have been formed on most of the fins. Nevertheless, the height of the fins is not entirely constant and there are visible cracks on the fins at certain locations. The reason for this might be related to a number of things such as a very small misalignment of the HSQ lines, imperfections in the HSQ lines, cleanliness of the substrate, or to dislocations in the crystal lattice due to lattice mismatch. It is unknown how sensitive the {110} facet formation is with respect to the orientation of the HSQ lines. It is clearly seen from figure 4.6 a) that the InGaAs fins at $60 - 62°$ appear to be of good quality (even those at $57 - 59°$ look acceptable). It is although unknown how the facets would change at smaller angular step sizes ($< 1°$). It is maybe possible that InGaAs fins with {110} facets are formed within a range of a few degrees whereas InGaAs fins with perfect {110} facets only appear at exactly the correct angle. The cracks may also be a result of imperfections in the HSQ lines, such as rough or uneven sidewalls. This might be a result from a bad resist, failed exposure, or improper development. Small imperfections and roughness on the HSQ lines might thus potentially disturb the growth and form fractures on the InGaAs fins.

Lastly, it is also possible that the irregularities on the fins is a result of defect formation in the crystal lattice. This might be related to the lattice mismatch of the fins which might not behave similar to the lattice mismatch for thin films. It was assumed that the fins would obtain a similar chemical composition as a thin film when grown during identical conditions. This does not however have to be true, the chemical composition in the fins might be different than for thin films. If this is the case it also matters how the chemical composition in the fins is different. Compared to the previously measured thin film composition of $x = 66\%$, a higher indium content in the fins would result in increased lattice mismatch and thus higher defect density.

4.4.2 Misaligned growth mask

If the growth mask is misaligned with respect to the {110} facets, the sidewalls of the resulting InGaAs fins will not be smooth. The hexagonal symmetry of the {110} facets will produce sidewalls that follow zigzag patterns. This is shown in figure 4.7 a) whereas a hexagon with equivalent {110} facets is shown in figure 4.7 b).

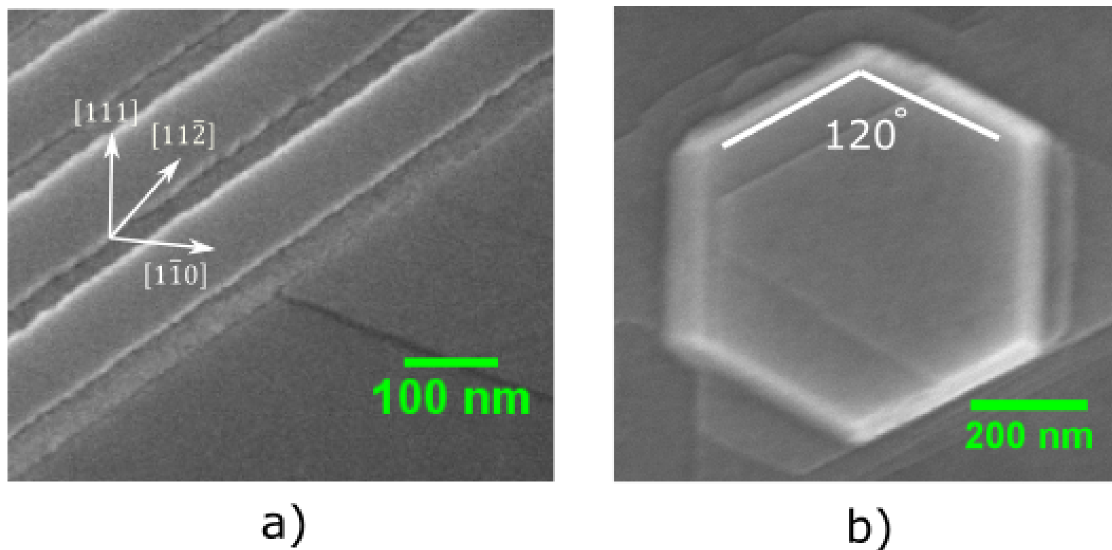

Figure 4.7: Scanning electron micrographs of a) InGaAs fins with zigzag sidewalls and b) hexagon with {110} facets.

The zigzag pattern arises since the HSQ lines are not aligned to any of the straight sides of the hexagon in figure 4.7 b). It can be thought of as if the sidewalls in figure 4.7 a) consist of many overlapping {110} faceted hexagons that are misaligned to each other. These kind of defects were observed for fins that were a few degrees

off from the correct orientation on the substrate. The white arrows in figure 4.7 a) roughly indicate the misalignment of the sidewalls of the grown InGaAs fins relative to the $[1\bar{1}0]$ direction.

4.4.3 FIB cross sections

In order to investigate the facets of the sidewalls as well as to measure the height and width of the fins, FIB cross sections were made. This was carried out by slicing the fins using FIB milling as described in section 2.3.1. Prior to the milling, the HSQ lines were removed using a buffered oxide etch (BOE). Additionally, since the ion beam sputters material, the InGaAs fins had to be covered with a protective metal layer prior to the milling. This was performed by locally depositing platinum on top of the fins using electron beam assisted deposition. The electron beam in the SEM was used to crack platinum hexacarbonyl molecules above the sample surface which resulted in the deposition of platinum.

The result of the FIB milling is shown in figure 4.8 where four samples are presented. All of the samples were grown at different V/III ratios but with identical gas phase compositions and growth times. The V/III ratio was set to 5, 10, 18, and 30 and is given in each of the figures. From figure 4.8 it is evident that the fins grown at V/III ratios of 10, 18, and 30 have laterally overgrown the HSQ mask. This is indicated by the small gap at the bottom of the fins and is pointed out by arrows in each of the figures. The gap represents the position of the HSQ mask that was present during the growth. The gap is an indication that the lateral growth of the fins, i.e. the growth of the sidewalls, have extended over the growth mask. This is clearly visible for the fins grown at V/III ratios of 10, 18, and 30 whereas it is barely visible for the fins growth at a V/III ratio of 5. This suggests that the lateral growth rate of the {110} facets is increased as the V/III ratio is increased and thus results in mask overgrowth. This is also reflected in the width and height of the fins which is plotted in figure 4.9 as a function of the V/III ratio. The widths and heights that are presented in figure 4.9 are averaged measurements from several fins (not only the fins shown in figure 4.8). The plot in figure 4.9 shows that the average height of the fins increases as the V/III ratio is decreased. It also shows that the width of the fins is minimized for low V/III ratios. This confirms that the relative growth rate of the {111}B facets compared to the {110} facets increases as the V/III ratio is decreased. This explains the

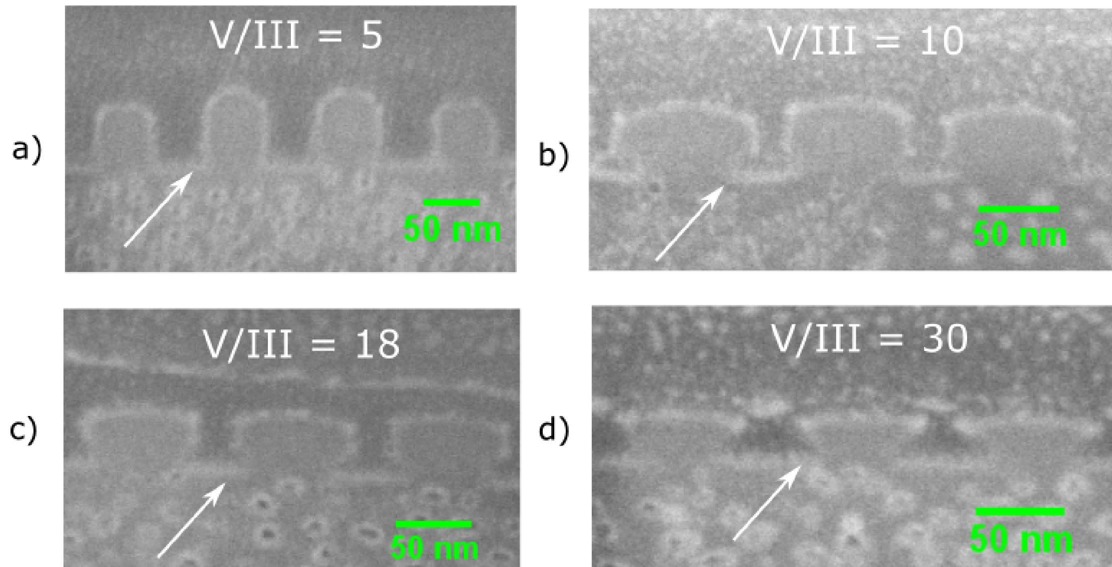

FIGURE 4.8: Scanning electron micrographs of sliced InGaAs fins grown with V/III ratios of 5, 10, 18, and 30. The arrow in each image indicates the mask overgrowth (if any).

behavior of the dimensions of the fins as the V/III ratio is varied. The conclusion from figure 4.8 and 4.9 is that InGaAs fins that are at least 65 nm high and with vertical sidewalls can be epitaxially grown on InP(111)B at low V/III ratios. This is attributed to the maximized relative growth rate between the {111}B and {110} facets that occurs at low V/III ratios. The width of the fins is determined by the spacing of the HSQ lines in the growth mask but the overgrowth and height is controlled by the V/III ratio.

4.4.4 Growth of higher fins

The growth time for the samples presented in figure 4.8 was set to 30 seconds. Due to the successful growth of fins at low V/III ratios such as the fins in figure 4.8 a), an additional sample was grown with a longer growth time. The V/III ratio was identical (5) and the growth time was increased to 60 seconds. The purpose of this attempt was to investigate the properties of the fins as the growth time was increased. Since the growth conditions were unchanged, the longer growth time was expected to result in increased growth on both the {111}B and {110} facets. The relative growth rates of the {111}B and {110} facets was however expected to remain unchanged. The initial hypothesis was that the fins would grow higher and possibly achieve a higher aspect ratio.

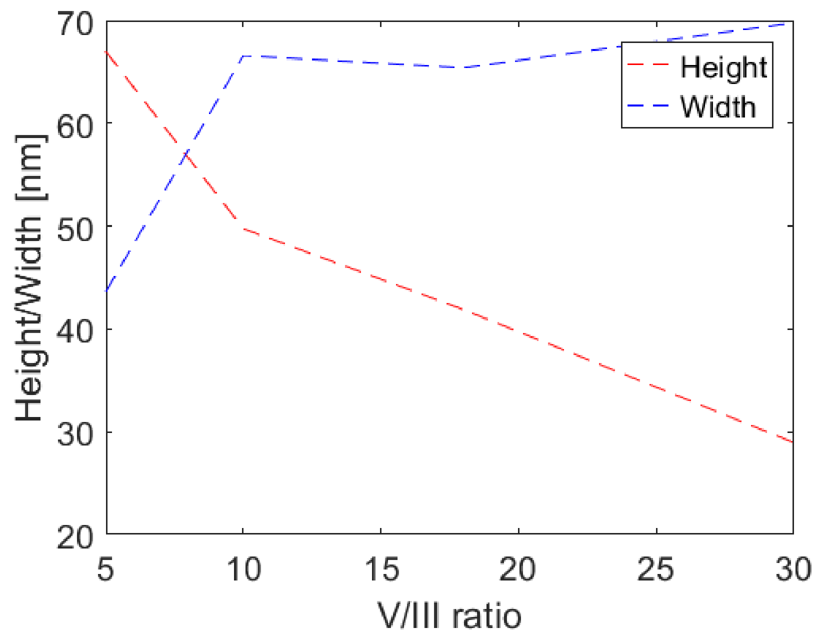

FIGURE 4.9: Plot of the average height and width of InGaAs fins grown at different V/III ratios.

The result of the FIB cross section is shown figure 4.10. It is evident that the fins have grown higher than the fins in figure 4.8 a). The height of the highest fin in figure 4.10 was measured to be 117 nm compared to 83.5 nm for the highest fin in figure 4.8 a). The widths were also compared and were found to increase from 42 nm to 67.5 nm as the growth time was longer (measured from the highest single fin in figure 4.8 a) and 4.10). The resulting aspect ratio of the highest fin in figure 4.8 is thus 1.98 whereas it is 1.73 for the highest fin in figure 4.10. In summary, by extending the growth time the fins grew 33.5 nm higher and 25.5 nm wider. Those numbers follow the expected pattern that the {111}B facets would grow faster than the {110} facets. The difference between the growth rates was however expected to be bigger than what was achieved. According to those numbers, the fins almost increased their width and height by the same amount resulting in a lower aspect ratio. The increase in the width can be attributed to the mask overgrowth which is clearly visible in figure 4.10 and is pointed out by the arrow. This was not observed for the fins in figure 4.8 a). There is therefore a limit of how high the fins can be grown without overgrowing the mask and this limit was evidently reached during the growth of the fins in figure 4.10. It is possible that an even lower V/III ratio could have compensated for the long growth time and thus a high aspect ratio could have been maintained. In conclusion, it is possible to produce $>$ 100 nm high InGaAs fins with vertical {110} faceted sidewalls. If a

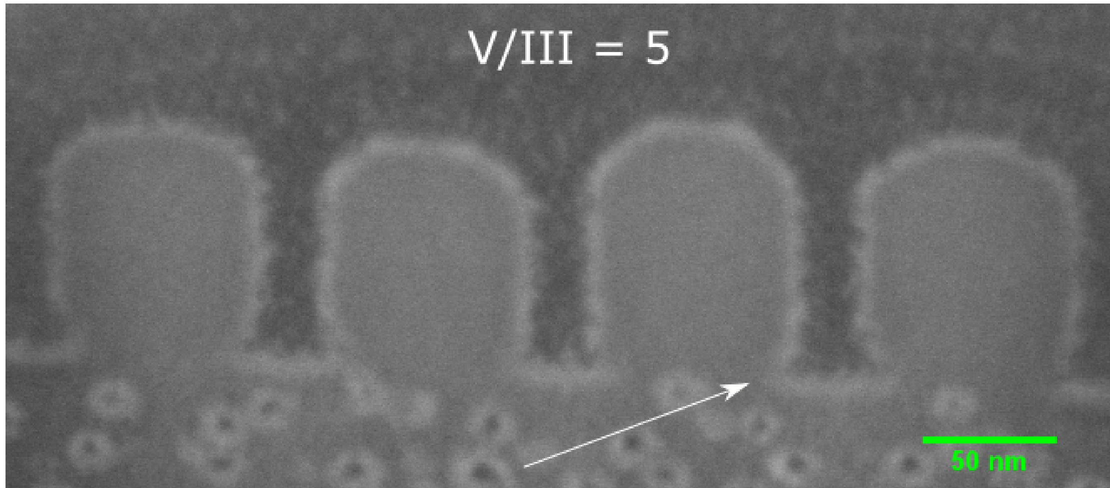

Figure 4.10: Scanning electron micrograph of sliced InGaAs fins grown during 60 seconds at a V/III ratio of 5.

high aspect ratio is to be maintained, there is however a limit on the height of the fins which is determined by the mask overgrowth. The width of the fins is initially controlled by the HSQ mask and high aspect ratio fins can be achieved as long as no mask overgrowth occurs. As the fins start to laterally overgrow the mask, the aspect ratio will decrease and thus limit the height of fins with the width defined by the mask.

4.4.5 Possible issues of the facet selective growth

Figure 4.11 shows an array of InGaAs fins grown identically to the fins in figure 4.10 (during 60 seconds). It can be seen in figure 4.11 that the height of the fins vary considerably along the length of the fins. This was not observed for the fins in figure 4.6 which were grown during 30 seconds. Even though the maximum height of the fins in figure 4.11 were increased when grown during 60 seconds, the height variation also increased which led to the zigzag shape on the top. Additionally, a new set of facets seemed to have formed as the fins were grown for 60 seconds. This was already seen on some of the fins in figure 4.10 where the sidewalls are inclined towards the {111}B facet. The same thing can also be seen in figure 4.11 and is pointed out by the arrow. It is evident that the initial {110} facets have grown away and that a new set of facets have been formed. This is very apparent in figure 4.10 and 4.11 whereas it not completely clear from figure 4.6 b) and 4.8 a). The new facets are inclined at approximately $45 - 50°$ relative to the {110} facets and might thus be {201} facets. It is possible that these facets might eventually

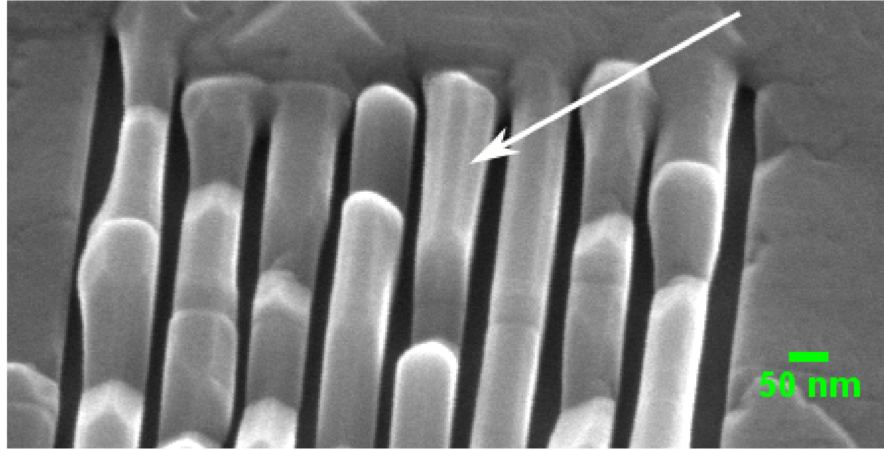

FIGURE 4.11: Scanning electron micrograph of an array of InGaAs fins suspected to suffer from defects.

limit the height of fins as the {111}B are grown away. It can be seen in figure 4.10 that the {111}B facets on the top of the fins becomes smaller as the new potential {201} facets are formed. These facets might therefore set a maximum height limit of InGaAs fins grown on InP(111)B.

It is possible that the height variations of the fins in figure 4.10 is connected of the formation of defects within the crystal lattice. According to the critical thickness estimation performed in appendix A, thin films with a chemical composition of $In_{0.66}Ga_{0.34}As$ on InP(001) has a critical thickness of approximately 200-300 nm. For simplicity, it is assumed that the critical thickness estimation for InP(001) is similar for InP(111)B. It is thus assumed that epitaxial thin films on InP(111)B will experience similar critical thicknesses as on InP(001). As previously discussed, the chemical composition of grown InGaAs fins might not have the same chemical composition as for thin InGaAs films. If this is the case, the critical thickness of the fins will different from that of thin films. Recent work in the Nanoelectronics group at EIT LTH showed that InGaAs fins grown on InP(001) contained more indium than planar InGaAs films when grown identically [19]. Using photoluminescence (PL) and Raman spectroscopy they demonstrated a shift in the InGaAs composition of the fins towards higher indium contents. Specifically, the thin films consisted of $In_{0.63}Ga_{0.37}As$ whereas the fins achieved a composition of $In_{0.85}Ga_{0.15}As$. The composition shift in the fins was explained by a local change of growth kinetics and diffusion, such as the flow of precursors, due to the HSQ growth mask. Due to the similarities in our work, such as HSQ growth mask and growth process, it is possible that the same effects are present in this work too. Since the thin InGaAs films grown in this work consisted of $In_{0.66}Ga_{0.34}As$, it is possible

that the InGaAs fins have compositions higher than that, towards $In_{0.85}Ga_{0.15}As$. According to the model in appendix A, compositions around $In_{0.85}Ga_{0.35}As$ have critical thicknesses of approximately 60 nm. It is therefore possible that the fins grown during 30 seconds were slightly above the critical thickness whereas the fins grown during 60 seconds were far above. This potentially explains why the fins in figure 4.11 suffer from severe height variations due to defects compared to the fins in figure 4.6.

Chapter 5

Conclusion and outlook

This thesis has demonstrated epitaxial growth of InGaAs fins on InP(111)B using facet selective growth. The results have shown that the formation of high-aspect ratio InGaAs fins with vertical sidewalls consisting of {110} facets is pronounced at low V/III ratios. Approximately 117 nm high InGaAs fins with vertical sidewalls were obtained at a V/III ratio of 5. Due to the slow growth rate of the {110} facets, high-aspect ratio InGaAs fins can be fabricated using a growth mask with closely spaced HSQ lines.

The work presented in this thesis opens up for continued research that may eventually lead to complete FinFETs consisting of InGaAs fins grown on InP(111)B. Reaching complete FinFETs however first requires improvements and characterization of the facet selective grown InGaAs fins. The improvements might involve growth of lattice matched InGaAs fins with reduced defects as well as investigation of the height limit due to the disappearing {111}B facets. In-line HRXRD as well as PL and Raman spectroscopy could be used to determine the composition of the actual fins and thus enable growth of lattice matched fins. The growth of lattice matched fins is of the essence if the goal is to obtain high-aspect ratio fins that are free from defects. The trade-off would then be in terms of electron mobility since complete lattice match between InGaAs and InP forces the indium composition in InGaAs to be 53 %. A high indium composition is on the other hand favorable since the electron mobility of InAs is higher than for GaAs. It is perhaps, depending on the application, possible to optimize the indium composition such that defect-fee fins of sufficiently high aspect ratio and with maximized mobility

can be fabricated, i.e. allow the fins to be slightly lattice mismatched so that a higher mobility can be achieved.

In conclusion, epitaxial growth of InGaAs fins on InP(111)B is a promising fabrication method for the channel in InGaAs FinFETs. Since no plasma etching process is required, there is no risk of damaging the surface of the InGaAs fins during the fabrication and the high electron mobility offered by InGaAs is thus not jeopardized. This minimizes the surface scattering of electrons in InGaAs FinFETs and allows for high drain currents at low supply voltages. Additionally, the possibility to obtain high-aspect ratio InGaAs fins may further increase the maximum drain current which makes InGaAs fins grown on InP(111)B more attractive than InGaAs fins on InP(001). By changing the substrate from InP(001) to InP(111)B, InGaAs FinFETs might experience a significant performance boost and eventually find applications in electronic devices.

Appendix A

Modeling the critical thickness of InGaAs on InP

The critical thickness of an epitaxial InGaAs film grown on InP(001) can be estimated using the Matthews-Blakeslee model as described in [20]. Only a simple description of the model is given here whereas the reader is referred to the reference for further information. Here, the strain in an epitaxial InGaAs film is assumed to be constant throughout the entire film of thickness h. The strain energy per unit area in the strained InGaAs film is given by

$$E_s = 2G\left(\frac{1+\nu}{1-\nu}\right)\epsilon^2 h \tag{A.1}$$

where G is the shear modulus, ν is the Poisson ratio, and ϵ is the lattice mismatch. The sheer modulus G is defined as the ratio between the sheer stress and the sheer strain in the film whereas the Poisson ratio is the ratio between the lateral strain and the vertical strain in the film. The lattice mismatch between the film and the substrate is defined as

$$\epsilon = \frac{a_e(x) - a_s}{a_s} \tag{A.2}$$

where a_e and a_s are the lattice parameters for the epitaxial InGaAs film and the InP substrate respectively. The lattice parameter $a_e(x)$ of InGaAs is in turn dependent on the actual composition x of the $In_xGa_{1-x}As$ film.

It is furthermore assumed that misfit dislocations in a film will start to form when the strain energy of the lattice equals the energy of the dislocations. There are several kinds of dislocations that are formed at different strain energies. In this model, screw dislocations are assumed to be formed first since they have the smallest energy density. An expression for the energy density of screw dislocations is given as

$$E_D \simeq \left(\frac{G\|b\|^2}{8\pi\sqrt{2}a_e(x)}\right)\ln\left(\frac{h}{b}\right) \tag{A.3}$$

where $\|b\|$ is the magnitude of the Burgers vector and $a_e(x)$ is the lattice constant of the epitaxial film. The magnitude of the Burgers vector $\|b\|$ represents the magnitude of the lattice distortion resulting from a dislocation and is given by

$$\|b\| = \frac{a(x)}{2}\sqrt{h^2+k^2+l^2} \tag{A.4}$$

where h, k, and l are the miller indices of the growth direction.

It can be seen that both the strain energy density in equation A.1 and the dislocation energy density in equation A.3 depends on the thickness h of the epitaxial film. There is thus a certain critical thickness h (referred to as h_c) at which the strain energy equals the dislocation energy. This critical thickness h_c can be solved for by equating equations A.1 and A.3 which yields

$$h_c \simeq \left(\frac{1-\nu}{1+\nu}\right)\left(\frac{1}{16\pi\sqrt{2}}\right)\left(\frac{\|b\|^2}{a_e(x)}\right)\left(\frac{1}{\epsilon^2}\right)\ln\left(\frac{h_c}{b}\right) \tag{A.5}$$

Equation A.5 has to be solved numerically for all of the possible lattice parameters $a_e(x)$ of InGaAs in order to obtain the critical thickness as a function of composition x. The InGaAs lattice parameters were in the range of $a_{\mathrm{GaAs}} < a_{\mathrm{InGaAs}} < a_{\mathrm{InAs}}$ whereas the magnitude of the Burgers vector $\|b\|$ was calculated according to equation A.4. The result of solving equation A.5 numerically is shown in figure A.1 where the critical thickness h_c is plotted as a function of $In_xGa_{1-x}As$ composition x. It can be seen in figure A.1 that the critical thickness is discontinuous near compositions of $x \simeq 0.5$ of an epitaxial InGaAs film. This is because $In_{0.53}Ga_{0.47}As$ is perfectly lattice matched to InP and no lattice mismatch is present. Thick defect-free films of $In_{0.53}Ga_{0.47}As$ can thus be grown on InP(001). As the composition

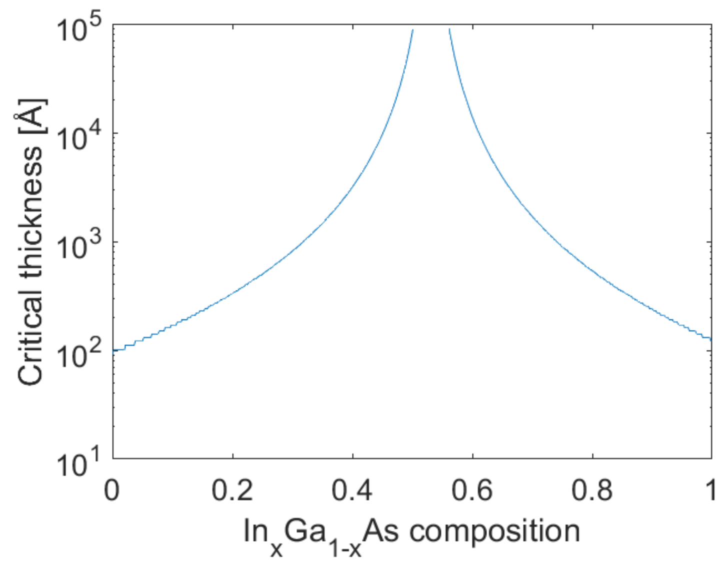

FIGURE A.1: Critical thickness in Å of epitaxial films of InGaAs grown on InP(001) as a function of $In_xGa_{1-x}As$ composition x.

deviates from $x = 0.53$, the critical thickness rapidly decreases towards only a few nm.

Appendix B

Formation of the growth mask

B.1 Resist spin coating

Before the spin coating of the resist, the InP substrates were cleaned in a wet process using acetone and isopropanol in order to remove organic contamination from the surface. A second cleaning step was also performed using an ozone cleaner during 10 minutes which further cleaned the surface using ozone and UV-light [21]. The HSQ e-beam resist was prepared by diluting the original resist (XR-1541-006 from *Dow Corning*) in MIBK (methyl isobutyl ketone) at a 3:1 ratio of MIBK:HSQ. This was done in order to achieve a certain thickness of the resist after exposure. With this specific dilution and with the spin coating recipe, exposed HSQ areas will have a thickness of approximately 20 nm. Exposure to the electron beam induces chemical reactions in the HSQ resist which results in the formation of SiO_2 which make up the printed pattern. The reason for using HSQ as e-beam resist for the growth mask is because the SiO_2 does not melt at high temperatures during epitaxial growth.

B.2 Patterning

The dose deposited by the electron beam into the resist, measured in $\mu C/cm^2$, was found to be heavily dependent on the width and spacing of the HSQ lines. Several exposure tests were performed where the dose was varied over a large range in order to find the optimal dose. The exposure tests were inspected using SEM and

correctly exposed HSQ lines of 50 nm width and spacing were achieved for doses around 2700-4000 μC/cm^2.

B.3 Development

The development of patterned HSQ resist was carried out in a solution of 25 % tetramethylammonium hydroxide (TMAH). Initially, the development was performed in a bath of room temperature TMAH during 90 seconds followed by rinsing of the sample in water and isopropanol. The process was completed by blow drying the samples using nitrogen gas. The subsecuent epitaxial growth of InGaAs fins on HSQ growth masks developed using this process was found to be defective as shown in figure B.1. The surface in figure B.1 around the HSQ lines is broken and non-uniform and no smooth layer or fins have been formed. It was suspected that the defective growth originated from surface contamination consisting of leftover HSQ residues that were present between and around the HSQ lines. Inspection of the HSQ lines after development confirmed that the surface was covered by small particles as shown in figure B.2 a). A modified development process was therefore adopted according to [22] in which the TMAH was heated to 50°C and agitated using ultrasonic agitation. The ultra sonic agitation lasted for 90 seconds during which the resist was fully developed and resist residues were removed. The result of this development process is shown in figure B.2 b) where it can be seen that the surface between and around the HSQ lines is a considerably cleaner than in figure B.2 a). The development process using hot TMAH and ultra sonic agitation was therefore adopted as the standard development process for all samples in this thesis.

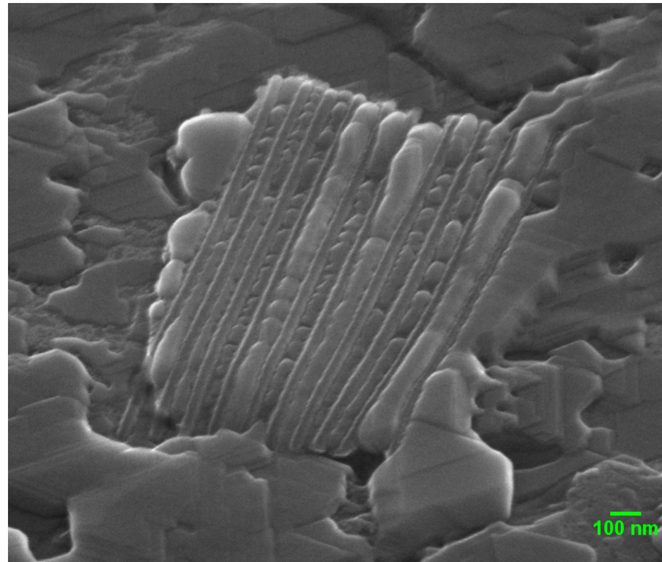

Figure B.1: Scanning electron micrograph of defective InGaAs around an array of HSQ lines.

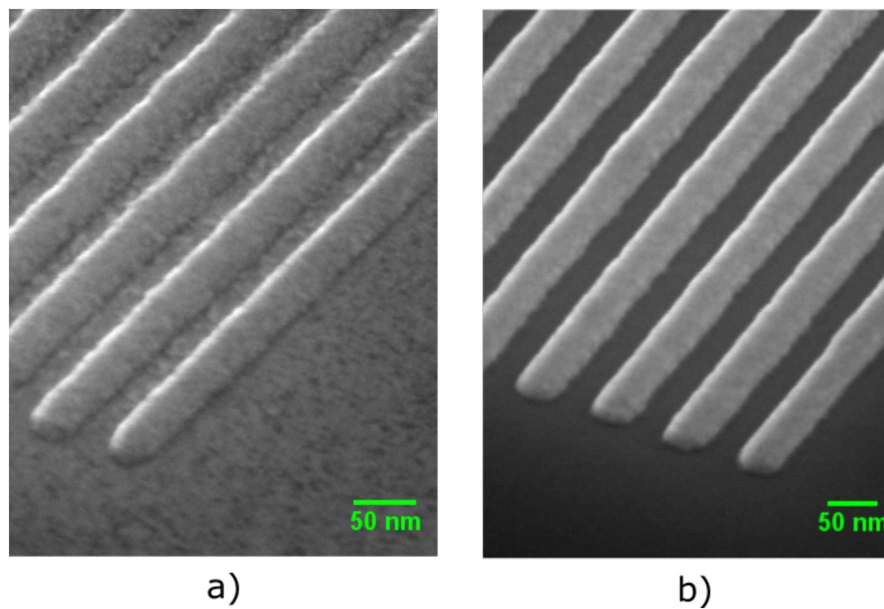

Figure B.2: Scanning electron micrographs of a) contaminated HSQ lines and b) clean HSQ lines.

Bibliography

[1] K. Ahmed and K. Schuegraf. Transistor wars. *IEEE Spectrum*, 48(11):50–66, November 2011. ISSN 0018-9235. doi: 10.1109/MSPEC.2011.6056626.

[2] M. h. Chi. Finfet technology: Overview and status at 14nm node and beyond. In *2016 China Semiconductor Technology International Conference (CSTIC)*, pages 1–3, March 2016. doi: 10.1109/CSTIC.2016.7464027.

[3] G. E. Moore. Cramming more components onto integrated circuits, reprinted from electronics, volume 38, number 8, april 19, 1965, pp.114 ff. *IEEE Solid-State Circuits Society Newsletter*, 11(5):33–35, Sept 2006. ISSN 1098-4232. doi: 10.1109/N-SSC.2006.4785860.

[4] Intel 22 nm technology. `http://www.intel.com/content/www/us/en/silicon-innovations/intel-22nm-technology.html`. Accessed: 2017-05-27.

[5] Keren J. Kanarik, Gowri Kamarthy, and Richard A. Gottscho. Plasma etch challenges for finfet transistors. *Solid State Technology*, 55, April 2012.

[6] K. Endo, S. Noda, M. Masahara, T. Kubota, T. Ozaki, S. Samukawa, Y. Liu, K. Ishii, Y. Ishikawa, E. Sugimata, T. Matsukawa, H. Takashima, H. Yamauchi, and E. Suzuki. Fabrication of finfets by damage-free neutral-beam etching technology. *IEEE Transactions on Electron Devices*, 53(8):1826–1833, Aug 2006. ISSN 0018-9383. doi: 10.1109/TED.2006.877035.

[7] Kazuhiko Endo, S. Noda, M. Masahara, T. Kubota, T. Ozaki, S. Samukawa, Yongxun Liu, K. Ishii, Y. Ishikawa, E. Sugimata, T. Matsukawa, H. Takashima, H. Yamauchi, and E. Suzuki. Damage-free neutral beam etching technology for high mobility finfets. In *IEEE InternationalElectron Devices Meeting, 2005. IEDM Technical Digest.*, pages 840–843, Dec 2005. doi: 10.1109/IEDM.2005.1609487.

[8] C. B. Zota, L. E. Wernersson, and E. Lind. $in_{0.53}ga_{0.47}as$ multiple-gate field-effect transistors with selectively regrown channels. *IEEE Electron Device Letters*, 35(3):342–344, March 2014. ISSN 0741-3106.

[9] C. B. Zota, L. E. Wernersson, and E. Lind. Single suspended ingaas nanowire mosfets. In *2015 IEEE International Electron Devices Meeting (IEDM)*, pages 31.4.1–31.4.4, Dec 2015. doi: 10.1109/IEDM.2015.7409808.

[10] C. B. Zota, L. E. Wernersson, and E. Lind. High-performance lateral nanowire ingaas mosfets with improved on-current. *IEEE Electron Device Letters*, 37 (10):1264–1267, Oct 2016. ISSN 0741-3106. doi: 10.1109/LED.2016.2602841.

[11] U.W. Pohl. *Epitaxy of Semiconductors: Introduction to Physical Principles*. Graduate Texts in Physics. Springer Berlin Heidelberg, 2013. ISBN 9783642329708. URL `https://books.google.se/books?id=DShEAAAAQBAJ`.

[12] W. Liu. *Fundamentals of III-V Devices: HBTs, MESFETs, and HFETs/HEMTs*. Wiley, 1999. ISBN 9780471297000. URL `https://books.google.se/books?id=edJpQgAACAAJ`.

[13] Gerald B. Stringfellow. 1 - overview of the {OMVPE} process. In Gerald B. Stringfellow, editor, *Organometallic Vapor-Phase Epitaxy (Second Edition)*, pages 1 – 16. Academic Press, San Diego, second edition edition, 1999. ISBN 978-0-12-673842-1. doi: http://doi.org/10.1016/B978-012673842-1/50004-1. URL `http://www.sciencedirect.com/science/article/pii/B9780126738421500041`.

[14] Gerald B. Stringfellow. 4 - source molecules. In Gerald B. Stringfellow, editor, *Organometallic Vapor-Phase Epitaxy (Second Edition)*, pages 151 – 209. Academic Press, San Diego, second edition edition, 1999. ISBN 978-0-12-673842-1. doi: http://doi.org/10.1016/B978-012673842-1/50007-7. URL `http://www.sciencedirect.com/science/article/pii/B9780126738421500077`.

[15] Gerald B. Stringfellow. 2 - thermodynamics. In Gerald B. Stringfellow, editor, *Organometallic Vapor-Phase Epitaxy (Second Edition)*, pages 17 – 111. Academic Press, San Diego, second edition edition, 1999. ISBN 978-0-12-673842-1. doi: http://doi.org/10.1016/B978-012673842-1/50005-3. URL `http://www.sciencedirect.com/science/article/pii/B9780126738421500053`.

[16] Gerald B. Stringfellow. 3 - physical processes occurring on the surface. In Gerald B. Stringfellow, editor, *Organometallic Vapor-Phase Epitaxy (Second Edition)*, pages 113 – 149. Academic Press, San Diego, second edition edition, 1999. ISBN 978-0-12-673842-1. doi: http://doi.org/10.1016/B978-012673842-1/50006-5. URL http://www.sciencedirect.com/science/article/pii/B9780126738421500065.

[17] Gerald B. Stringfellow. 7 - design of the {OMVPE} process. In Gerald B. Stringfellow, editor, *Organometallic Vapor-Phase Epitaxy (Second Edition)*, pages 319 – 389. Academic Press, San Diego, second edition edition, 1999. ISBN 978-0-12-673842-1. doi: http://doi.org/10.1016/B978-012673842-1/50010-7. URL http://www.sciencedirect.com/science/article/pii/B9780126738421500107.

[18] D.K. Bowen and B.K. Tanner. *X-Ray Metrology in Semiconductor Manufacturing*. CRC Press, 2006. ISBN 9781420005653. URL https://books.google.se/books?id=-gLOBQAAQBAJ.

[19] Cezar Zota, David Lindgren, Lars-Erik Wernersson, and Erik Lind. Quantized conduction and high mobility in selectively grown ingaas nanowires. 9 (10):9892–9897, 2015. ISSN 1936-086X. URL http://dx.doi.org/10.1021/acsnano.5b03318.

[20] D. J. DUNSTAN. Strain and strain relaxation in semiconductors. *Journal of Materials Science: Materials in Electronics*, 8(6):337–375, 1997. ISSN 1573-482X. doi: 10.1023/A:1018547625106. URL http://dx.doi.org/10.1023/A:1018547625106.

[21] J. Vig and J. LeBus. Uv/ozone cleaning of surfaces. *IEEE Transactions on Parts, Hybrids, and Packaging*, 12(4):365–370, Dec 1976. ISSN 0361-1000. doi: 10.1109/TPHP.1976.1135156.

[22] Yifang Chen, Haifang Yang, and Zheng Cui. Effects of developing conditions on the contrast and sensitivity of hydrogen silsesquioxane. *Microelectronic Engineering*, 83(4–9):1119 – 1123, 2006. ISSN 0167-9317. doi: http://doi.org/10.1016/j.mee.2006.01.167. URL http://www.sciencedirect.com/science/article/pii/S0167931706002607. Micro- and Nano-Engineering {MNE} 2005Proceedings of the 31st International Conference on Micro- and Nano-Engineering.